MNRAS 000, 1–20 (2022) Preprint 17 January 2022 Compiled using MNRAS LATEX style file v3.0

Systematic biases in determining dust attenuation curves through galaxy SED fitting

Jianbo Qin,[1⋆] Xian Zhong Zheng,[1,2†] Min Fang,[1,2] Zhizheng Pan,[1,2] Stijn Wuyts,[3] Yong Shi,[4,5] Yingjie Peng,[6] Valentino Gonzalez,[7,8] Fuyan Bian,[9] Jia-Sheng Huang,[10,11] Qiu-Sheng Gu,[4,5] Wenhao Liu,[1,2] Qinghua Tan,[1,2] Dong Dong Shi,[1] Jian Ren,[1,2] Yuheng Zhang,[1,2] Man Qiao,[1,2] Run Wen,[1,2] and Shuang Liu[1,2]

[1] *Purple Mountain Observatory, Chinese Academy of Sciences, 10 Yuanhua Road, Nanjing 210023, China*
[2] *School of Astronomy and Space Sciences, University of Science and Technology of China, Hefei 230026, China*
[3] *Department of Physics, University of Bath, Claverton Down, Bath BA2 7AY, UK*
[4] *School of Astronomy and Space Science, Nanjing University, Nanjing 210093, China*
[5] *Key Laboratory of Modern Astronomy and Astrophysics (Nanjing University), Ministry of Education, Nanjing 210093, China*
[6] *Kavli Institute for Astronomy and Astrophysics, Peking University, 5 Yiheyuan Road, Beijing 100871, China*
[7] *Chinese Academy of Sciences South America Centre for Astronomy, China-Chile Joint Centre for Astronomy, Camino del Observatorio 1515, Las Condes, Chile*
[8] *Centro de Astrofísica y Tecnologías Afines (CATA), Camino del Observatorio 1515, Las Condes, Santiago, Chile*
[9] *European South Observatory, Alonso de Cordova 3107, Casilla 19001, Vitacura, Santiago 19, Chile*
[10] *Chinese Academy of Sciences South America Center for Astronomy, National Astronomical Observatories, Chinese Academy of Sciences, Beijing 100101, China*
[11] *CAS Key Laboratory of Optical Astronomy, National Astronomical Observatories, Chinese Academy of Sciences, Beijing 100101, China*

arXiv:2201.05467v1 [astro-ph.GA] 14 Jan 2022

Accepted 2022 January 13. Received 2022 January 4; in original form 2021 November 23

ABSTRACT

While the slope of the dust attenuation curve (δ) is found to correlate with effective dust attenuation (A_V) as obtained through spectral energy distribution (SED) fitting, it remains unknown how the fitting degeneracies shape this relation. We examine the degeneracy effects by fitting SEDs of a sample of local star-forming galaxies (SFGs) selected from the Galaxy And Mass Assembly survey, in conjunction with mock galaxy SEDs of known attenuation parameters. A well-designed declining starburst star formation history is adopted to generate model SED templates with intrinsic UV slope (β_0) spanning over a reasonably wide range. The best-fitting β_0 for our sample SFGs shows a wide coverage, dramatically differing from the limited range of $\beta_0 < -2.2$ for a starburst of constant star formation. Our results show that strong degeneracies between β_0, δ, and A_V in the SED fitting induce systematic biases leading to a false A_V–δ correlation. Our simulation tests reveal that this relationship can be well reproduced even when a flat A_V–δ relation is taken to build the input model galaxy SEDs. The variations in best-fitting δ are dominated by the fitting errors. We show that assuming a starburst with constant star formation in SED fitting will result in a steeper attenuation curve, smaller degeneracy errors, and a stronger A_V–δ relation. Our findings confirm that the A_V–δ relation obtained through SED fitting is likely driven by the systematic biases induced by the fitting degeneracies between β_0, δ, and A_V.

Key words: dust, extinction – Galaxies: evolution – Galaxies: ISM – Galaxies: star formation

1 INTRODUCTION

Dust, which accounts for only a small fraction (∼1 per cent) of the interstellar medium (ISM) in star-forming galaxies (SFGs), can significantly change observables of the SFGs through absorbing and scattering stellar radiation (Galliano et al. 2018, and references therein). The size distribution of dust grains and their chemical compounds regulate the degree of absorption and scattering across wavelength, described as the dust extinction curve (Draine & Lee 1984; Draine 2003). Interstellar dust containing more small grains yields a steeper extinction curve (Weingartner & Draine 2001; Draine 2003; Hirashita 2012; Asano et al. 2014; Hou et al. 2017; Aoyama et al. 2017). In practice, extinction can be quantified via measuring light from a point source behind a dust screen. For an extended source like a galaxy, where dust and stars are mixed, dust attenuation is used

⋆ jbqin@pmo.ac.cn
† xzzheng@pmo.ac.cn

© 2022 The Authors

to describe the deviation between the observed and the intrinsic stellar emission. The dust attenuation curve relies on not only the properties of the interstellar dust but also the geometry by which stars and dust are spatially distributed in the galaxy (Witt & Gordon 1996, 2000; Seon & Draine 2016; Narayanan et al. 2018; Lin et al. 2021). Understanding the mechanisms/processes shaping the dust attenuation curve will provide key insights into the dust and structural evolution of galaxies.

It is well known that the shape of the dust extinction/attenuation curve varies significantly from one galaxy to another, including the Milky Way (MW; Fitzpatrick & Massa 1986; Cardelli et al. 1989; Ferreras et al. 2021), the Large Magellanic Cloud (LMC) and the Small Magellanic Cloud (SMC) (Pei 1992; Gordon et al. 2003), M31 (Clayton et al. 2015), as well as some galaxies in the nearby Universe (e.g. Calzetti et al. 2000; Gordon et al. 2003; Wild et al. 2011; Calzetti et al. 2021; Rezaee et al. 2021) and the distant Universe (e.g. Kriek & Conroy 2013; Reddy et al. 2015, 2020; Shivaei et al. 2020; Kashino et al. 2021). The variation is mostly attributed to the slope (or steepness) and the amplitude of the 2175 Å bump. The former is primarily governed by the size distribution of dust grains and the star-dust geometry (Hirashita 2012; Narayanan et al. 2018), while the latter is probably caused by the graphite grains (e.g., Mathis 1994) or the polycyclic aromatic hydrocarbons (PAH; Weingartner & Draine 2001; Draine 2003). The extinction/attenuation curves of the LMC and SMC are steeper than those of the MW and nearby starburst galaxies, and the 2175 Å bump is observed in the MW and LMC but not in the SMC and nearby starbursts.

In the past decade, many efforts have been devoted to addressing the relationships between the features of dust attenuation curves and galaxy properties. The slope of the dust attenuation curve was reported to depend on stellar mass (Zeimann et al. 2015), star formation rate (SFR; Teklu et al. 2020), specific SFR (sSFR = SFR/M_*; Reddy et al. 2015; Battisti et al. 2017b; Rezaee et al. 2021), metallicity (Battisti et al. 2017b; Shivaei et al. 2020), as well as inclination (Wild et al. 2011; Battisti et al. 2017a, 2020). However, some correlations remain controversial or inconsistent with each other, partially due to inconsistent datasets and methods used for drawing the conclusions.

Recently, an increasing number of studies determined the dust attenuation curves of galaxies by taking the slope of the curves as a free parameter in modelling galaxy broadband spectral energy distribution (SED). The SED fitting approach is applied to a large sample of galaxies. With this approach, an anti-correlation between the best-fitting slope of dust attenuation curves (e.g., UV-to-optical attenuation ratio $S \equiv A_{\rm FUV}/A_{\rm V}$) and dust column density (as approximately traced by $A_{\rm V}$) in SFGs has been established, in the sense that a flatter attenuation curve is linked with a higher $A_{\rm V}$ (e.g. Kriek & Conroy 2013; Arnouts et al. 2013; Salmon et al. 2016; Leja et al. 2017; Salim et al. 2018; Decleir et al. 2019; Battisti et al. 2020). Theoretical investigations with radiative transfer models also predicted this $A_{\rm V}$–slope relation (Witt & Gordon 2000; Chevallard et al. 2013; Narayanan et al. 2018; Trayford et al. 2020). Salim & Narayanan (2020, hereafter S20) pointed out that $A_{\rm V}$ is the dominant driver of the attenuation curve slope, and at a fixed $A_{\rm V}$ (a proxy of dust column density) the slope does not show dependence on other galaxy parameters. If confirmed, this relation could play a key role in describing the variation of dust attenuation curves.

However, a fitting degeneracy exists between the two quantities involved in the $A_{\rm V}$–slope relation. Given that $A_{\rm V}$ is also used to define the attenuation curve slope (e.g., $A_{\rm FUV}/A_{\rm V}$), any errors in SED fitting that enlarge $A_{\rm V}$ would lead to a decrease of $A_{\rm FUV}/A_{\rm V}$, i.e. a flatter dust attenuation curve, when other parameters remain unchanged (Salmon et al. 2016). This issue was addressed in S20, showing that the degeneracy error from the given error ellipse (their Figure 9) is insignificant compared with the global relationship. By modelling the UV to NIR SEDs of star-forming regions in the SMC, Hagen et al. (2017) found a strong degeneracy between best-fitting $A_{\rm V}$ and attenuation curve slope (parameterized by $R_{\rm V}$[1]). It is worth noting that there is a high degree of degeneracy between the star formation histories (SFHs) and dust attenuation curves adopted in SED fitting (Calzetti et al. 2021). The determination of the attenuation curve is sensitive to the adopted SFHs in the fitting (Burgarella et al. 2005; Koprowski et al. 2020; Calzetti et al. 2021). Considering the fitting degeneracy is largely unexplored, a thorough investigation is demanded to examine if the $A_{\rm V}$–slope relation is largely shaped by the fitting degeneracy.

In this work, we aim to qualify the influence of fitting degeneracy on the well-established relation between $A_{\rm V}$ and attenuation curve slope. We use the observed data with secure measurements from the far-ultraviolet (FUV) to the far-infrared (FIR) to perform energy-balance fitting when modelling observed galaxy SEDs. In Section 2, we briefly describe the galaxy sample and data used for our analysis. We introduce the parameters of our SED fitting in Section 3. Section 4 presents our results of the fiducial fit configuration, while the results of a constant starburst fit configuration that is consistent with previous studies are given in Section 5 for comparison. We discuss our results in Section 6 and give a summary in Section 7. A standard ΛCDM cosmology with $H_0 = 70\,{\rm km^{-1}\,Mpc^{-1}}$, $\Omega_\Lambda = 0.7$, and $\Omega_{\rm m} = 0.3$ and a Chabrier (2003) Initial Mass Function (IMF) are adopted throughout the paper.

2 SAMPLE AND DATA

2.1 Sample selection

We carry out our investigation using the data from the Galaxy And Mass Assembly (GAMA) Survey, [2](Driver et al. 2009, 2011). GAMA is an optical comprehensive spectroscopic redshift survey over a 286 $\deg^2$ sky area divided into five different regions (with a limiting magnitude $r_{\rm petro} < 19.8$ mag) using the Anglo Australian Telescope's AAOmega wide-field facility (Driver et al. 2011; Hopkins et al. 2013; Liske et al. 2015).

The GAMA survey fields have extensive imaging data from the FUV to the FIR. These data come from different surveys: GALEX Medium Imaging Survey (GALEX MIS;

[1] $R_{\rm V} = A_{\rm V}/(A_{\rm B} - A_{\rm V})$

[2] http://www.gama-survey.org/dr3 and all the GAMA value-added catalogues used in this work can be found in http://www.gama-survey.org/dr3/data/cat/

Martin et al. 2005); the Sloan Digital Sky Survey (SDSS DR7; Abazajian & et al. 2009), the VIsta Kilo-degree INfrared Galaxy survey (VIKING; de Jong et al. 2013); the Wide-field Infrared Survey Explorer (WISE; Wright et al. 2010) and the Herschel Astrophysical Terahertz Large Area Survey (*Herschel*-ATLAS; Eales et al. 2010). These data were collected and released to the public by Driver et al. (2016) through the GAMA Panchromatic Data Release. The software LAMBDAR[3] was used to measure fluxes from the image data of 21 bands (FUV, NUV, u, g, r, i, z, Z, Y, J, H, K_s, 3.4, 4.5, 12, 22, 100, 160, 250, 350, and 500 μm) (see Wright et al. 2016, for more details). Elliptical apertures given by SExtractor were adopted to conduct photometry on the PSF-matched images, and corrections for the contamination by blended objects were employed. In short, the GAMA datasets provide multi-band photometric catalogues for a large sample of spectroscopically-identified nearby galaxies with $r_{\rm petro} < 19.8$ mag. We use the datasets to measure the galaxy attenuation parameters through SED modelling based on the energy balance principle.

The original LAMBDAR photometric catalogues contain 219 458 galaxies. Of them, 116 261 sources have $r_{\rm petro} < 19.8$ mag and a reliable redshift measurement (nQ $\geq$ 3). Both $r_{\rm petro}$ and nQ are taken from the TilingCat dataset. We limit targets over $0.07 < z < 0.2$. The lower limit of $z > 0.07$ is chosen following Kewley et al. (2005) to ensure the GAMA/AAT 2″ fibre takes > 20 per cent of the total star light of a typical galaxy and minimize the potential differences between nuclear and global galaxy properties. The upper limit of $z < 0.2$ is set to minimize evolutionary effects. There are 53 182 GAMA galaxies in this redshift range. We also exclude faint sources with stellar masses less than 10^9 $M_\odot$. The stellar masses are from StellarMasses dataset, measured by fitting the observed u to K_s-band photometric data (Taylor et al. 2011). There are 52 517 galaxies that meet our selection criteria.

Secure detections in multiple bands (including the FUV and the FIR) are needed for a robust determination of galaxy attenuation parameters through energy-balance SED fitting. Firstly, we select galaxies with a signal-to-noise ratio (S/N) greater than three in all bands from FUV to K_s,[4] leaving 17 796 out of 52 517 galaxies. Galactic extinction was corrected for all fluxes from FUV to K_s using the Schlegel et al. (1998) MW dust maps (Wright et al. 2016). To securely measure dust emission, we focus on the target galaxies with good detections (S/N > 3) in at least one of five *Herschel* PACS and SPIRE bands, leaving 8 531 galaxies with an FIR detection rate of 48 per cent. It is worth mentioning that the S/N cut in the FIR likely biases our sample selection towards galaxies being more dusty. Since we focus on investigating the parametrized relations and the sample still retain a dynamical range of nearly one order of magnitude in A_V ([0.1, 1.5] mag), the FIR selection cut will not significantly affect our results.

We also make use of WISE 12 μm and 22 μm data, if available, to improve the measure of total infrared (IR) luminosity (8–1000 μm). Most of our galaxies detected by *Herschel* have secure detections in either WISE 12 μm or 22 μm (S/N > 3, the detection rate is ∼83 per cent). We measure the IR luminosity via best-fitting the observed IR data points with the IR SED templates from the dust radiation model by Draine & Li (2007). We let the PAH fraction vary from 0.47 to 4.58, the minimum radiation field $U_{\rm min} = [0.1, 25]$, the maximum radiation field $U_{\rm max} = [10^3, 10^6]$, and the fraction illuminated from $U_{\rm min}$ to $U_{\rm max}$ is [0, 1]. If the IR bands which fall below 3 σ do have valid flux and error measurements, they are also included to constrain the IR luminosity measurements. For the bands without detections, the upper limits are used in the fitting. The typical error is ∼ 0.1 dex for the measured IR luminosities.

On the other hand, AGN activity may play a role in heating up the dust and thus contributing to the IR emission (Mullaney et al. 2011; Kirkpatrick et al. 2015), which increases the uncertainties in the modelling of SEDs. We select 'star-forming' galaxies without signs of nuclear activity based on the BPT diagram (Baldwin et al. 1981). This requires good measurements of the emission line fluxes including Hα, [N II], Hβ, and [O III]. These line fluxes are taken from the SpecLine dataset (Gordon et al. 2017). All lines have been measured by fitting the spectral line with a single Gaussian function. Following Salim et al. (2018), we require S/N > 10 for Hα and S/N > 2 for the remaining three lines. As pointed out, if we care about the line ratios (such as [N II]λ6584/Hα and [O III]λ5007/Hβ used in the BPT diagram as well as the metallicity determination), the usual cut S/N > 3 is too strict. When the S/N cut is relaxed, some sources with weak emission lines can be picked up and the sample size may increase. Finally, there are 2 764 sources satisfying our S/N cuts and classified as SFGs following the criteria given by Kauffmann et al. (2003).

The gas-phase metallicity, parameterized by Oxygen abundance O/H, is estimated from the N2 method using the formula given by Pettini & Pagel (2004) as

$$12+\log({\rm O/H}) = 9.37+2.03\times{\rm N2}+1.26\times{\rm N2}^2+0.32\times{\rm N2}^3, \quad (1)$$

where N2 = log([N II]λ6584/Hα). The N2 method is adopted since the emission lines in N2 are also used to identify SFGs with the BPT diagram. Our metallicity measurements can be carried out for the entire sample without introducing any additional selection criteria. Equation 1 is valid over $-2.5 <$ N2 < -0.3, corresponding to $7.17 < 12 + \log({\rm O/H}) < 8.86$ (Pettini & Pagel 2004). In our analysis, we exclude 9 galaxies with N2 out of this range. This will not affect our results.

The half-light radius (R_e) and axial ratio (b/a) are taken from Kelvin et al. (2012), who presented a single-Sérsic two-dimensional model fits to SDSS images for 167 600 galaxies in the GAMA data base. In this work, we adopt the r-band half-light radius and axial ratio. Using structural parameters of other SDSS bands does not alter our conclusions. We consider the best-fitting reduced chi-square ($\chi^2_r \equiv \chi^2/N_{\rm dof}$, where $N_{\rm dof}$ is the number of degrees of freedom) in the range $0.5 < \chi^2_r < 1.5$ as reliable measurements for morphological and structural parameters. We select disc galaxies with Sérsic index less than two. For galaxies with a Sérsic index greater than two, their shapes tend to be more spheroidal (Padilla & Strauss 2008), and the axial ratio is no longer a good probe of the inclination. We also exclude 19 extreme edge-on galaxies with axial ratio less than 0.15 from our sample, as the scale heights of these galaxies will bias the linkage between inclination and axial ratio (Guthrie 1992). Our fi-

[3] http://gama-psi.icrar.org/LAMBDAR.php
[4] Here the VISTA/VIRCAM Z band is not included.

nal sample contains 2 291 SFGs over $0.07 < z < 0.2$ with secure detections in multiple bands, as well as the gas-phase metallicity and structural parameters.

2.2 Flux correction for inclination-dependent inhomogeneity

When calculating the total luminosity of a disc galaxy over a solid angle of 4π radians, we often assume that its radiation is homogeneous in all directions. However, the UV and optical radiation are attenuated by dust that is mostly distributed in the disc and thus the UV/optical radiation is no longer uniform in all directions. The observed UV/optical flux is dependent on inclination. In contrast, the IR radiation is nearly free from dust attenuation and thus evenly emits in all directions. As a consequence, the UV/optical flux is underestimated (overestimated) for the edge-on (face-on) galaxies. This induces a tension in balancing energy between the UV/optical and the IR in SED fitting. This tension might result in artificial effects on dust attenuation (see Doore et al. 2021, and references therein). More importantly, the bias in the observed fluxes is strongly wavelength-dependent, and consequently influences the dust attenuation curve. In our analysis, the observed fluxes (and luminosities) in FUV to K_s are corrected for the inclination-induced bias and the 'corrected' values (i.e. the fluxes averaged over the 4π solid angle) are used to construct the observed SEDs.

Consider a galaxy with a brightness distribution of $L_\lambda(\phi, \theta)$, where ϕ and θ are the azimuth angle ($[0, 2\pi]$) and polar angle($[-\pi/2, \pi/2]$), respectively. Then the corrected luminosity can be obtained as

$$\begin{aligned} L_{\lambda,\mathrm{corrected}} &= \frac{1}{4\pi}\int_0^{4\pi} L_\lambda(\phi,\theta)d\Omega, \\ &= \frac{1}{4\pi}\int_0^{2\pi} d\phi \int_{-\frac{\pi}{2}}^{\frac{\pi}{2}} L_\lambda(\phi,\theta)\sin(\theta)d\theta. \end{aligned} \tag{2}$$

For a disc galaxy that is rotationally symmetrical along the ϕ direction and symmetrical along the θ direction, then Equation 2 can be written as

$$\begin{aligned} L_{\lambda,\mathrm{corrected}} &= \int_0^{\frac{\pi}{2}} L_\lambda(\theta)\sin(\theta)d\theta, \\ &= \int_0^1 L_\lambda[cos(\theta)]d[cos(\theta)], \\ &\approx \int_0^1 L_\lambda(\mathrm{b/a})d(\mathrm{b/a}). \end{aligned} \tag{3}$$

The random projection of a disc galaxy in 4π results in a distribution of galaxy inclination over $[0, \pi/2]$ or $\mathrm{b/a} = [0, 1]$. The corrected luminosity can be calculated by integrating the luminosity distribution over the range of b/a.

Qin et al. (2019a) found there is a tight power-law relation between $\mathrm{IRX} = L_{\mathrm{IR}}/L_{\mathrm{UV}}$ and b/a. Since L_{IR} is not affected by inclination, it is equivalent to a power-law relation between b/a and L_{UV}. Hence, we assume that the axial ratio and luminosity of each band satisfy a power-law relation $L_\lambda \propto (\mathrm{b/a})^\eta$. If the luminosity of a galaxy viewed face-on ($\mathrm{b/a} = 1$) is L_λ^f, then the luminosity at any b/a should be

$$L_\lambda = L_\lambda^f \times (\mathrm{b/a})^\eta. \tag{4}$$

Considering the redshift range of our sample is rather narrow ($0.07 < z < 0.2$), we ignore the band-shifting effect. We then substitute Equation 4 into the Equation 3, and have

$$\begin{aligned} L_{\lambda,\mathrm{corrected}} &= \int_0^1 L_\lambda^f(\mathrm{b/a})^\eta d(\mathrm{b/a}) \\ &= L_\lambda^f/(1+\eta), \\ &= \frac{L_\lambda}{(1+\eta)(\mathrm{b/a})^\eta}. \end{aligned} \tag{5}$$

With the observed luminosity, axial ratio and the power-law index η, the corrected luminosity for each band can be derived accordingly. Qin et al. (2019a) developed a novel method to obtain the intrinsic relation between axial ratio and IRX. The dependence of IRX on IR luminosity, metallicity, galaxy size and axial ratio were quantified by minimizing the dispersion of IRX in fitting the data points with multiple power-law functions. Given that IR luminosity is not dependent on galaxy inclination, the correlation between b/a and IRX is governed by the correlation between b/a and L_{UV}.

Similarly, we use the same galaxy parameters to minimize the scatter of the luminosity in each band as,

$$L_\lambda = 10^\alpha \left(\frac{L_{\mathrm{IR}}}{10^{10}\,\mathrm{L_\odot}}\right)^\beta \left(\frac{R_e}{\mathrm{kpc}}\right)^{-\gamma} (\mathrm{b/a})^{-\eta}, \tag{6}$$

where α, β, γ, and η are power-law exponents respectively. Qin et al. (2019a) found that these indices depend on the gas-phase metallicity, as

$$X = c_X \log(Z/\mathrm{Z_\odot}) + \mathrm{d_X}, \tag{7}$$

X represents α, β, γ, or η, and c_X and d_X are their respective coefficients. By best fitting the luminosity in each band, we obtain η.

Figure 1 shows the best-fitting power-law index η as a function of metallicity. η decreases from FUV to K_s, indicating that radiation at a shorter wavelength is more affected by the increasing dust attenuation (and decreasing b/a). We find the metal-poor galaxies have smaller η, i.e. flatter inclination-luminosity relation. This is consistent with the results presented in Qin et al. (2019a). They pointed out that the low-metallicity SFGs are usually less massive and tend to be more spheroidal in morphology, and the axial ratio is no longer decided by inclination. At increasing wavelength, e.g. from FUV to K_s, the dependence of luminosity on metallicity becomes gradually weaker.

We use Equation 5 to derive the corrected flux from the measured flux in a given band. The flux error is also adjusted to match the conversion. The right panel of Figure 1 shows the corrected-to-observed flux ratio as a function of axial ratio for galaxies with Solar metallicity of $12 + \log(\mathrm{O/H}) = 8.69$. We can see that for edge-on galaxies (i.e., $\mathrm{b/a} = 0.2$), the corrected-to-observed flux ratio is 3 and 1.2 in FUV and K_s, respectively. And for face-on galaxies (i.e., $\mathrm{b/a} = 1$), the ratio becomes 0.5 and 0.8, respectively. The corrected flux approximately equals the observed flux when the axial ratio is between 0.4 and 0.6, varying with metallicity and wavelength. In other words, the correction is equivalent to rotating all galaxies to $\mathrm{b/a} \sim 0.4 - 0.6$. It is clear that the inclination effect is wavelength-dependent, and it may affect the further determination of the attenuation curve. We use the corrections given by Equation 5 to convert the observed fluxes into the corrected fluxes and perform further analyses with data corrected for the inclination effect.

By doing this correction, we obtain SEDs satisfying the energy balance. One caveat is that the correction still suffers

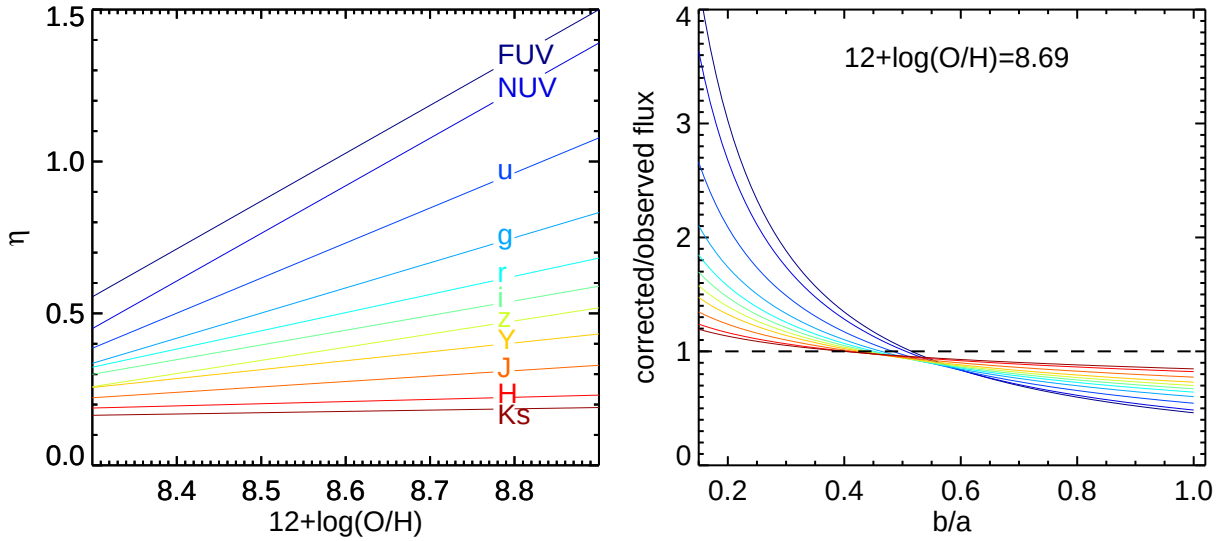


Figure 1. Left: Best-fitting power-law index η quantifying the inclination-dependent luminosity (Eq. 4) as a function of metallicity. The solid lines from top to bottom represent the relations from FUV to K_s. Right: The corrected-to-observed flux ratio as a function of axial ratio for galaxies with Solar metallicity. These lines are colour-coded by bands in the same way as in the left panel.

from some uncertainties. For example, we use the optical-band structure parameters (i.e., r-band) for the UV fluxes without corrections for the colour-gradient effects. We suspect that these uncertainties are marginal and our results are not significantly affected. In fact, our conclusions are insensitive to the inclination corrections. We verify that our main conclusions are not influenced even if using the inclination-uncorrected data.

3 FITTING GALAXY SEDS WITH CIGALE

We analyse the observed SEDs of our sample galaxies using the Code Investigating GALaxy Emission[5](CIGALE; Noll et al. 2009; Boquien et al. 2019). The basic idea of CIGALE is that the total energy radiated by the dust in the IR equals the total energy absorbed by the dust in the UV/optical. CIGALE combines a library of single stellar populations (SSP) and variable attenuation curves with SFH models to generate a large number of grid SED models to fit the observed data. The modelled SEDs are integrated into a set of filters and compared directly to the observations. The observations are assigned with an extra 10 per cent uncertainty (done by CIGALE itself) to account for the uncertainties from the models themselves (see Noll et al. 2009). The output parameters are measured with the Bayesian likelihood statistics method based on the probability distribution functions (PDFs). The best-fitting parameters and the corresponding uncertainties are the likelihood-weighted mean[6] and the standard deviation of all models. Details of CIGALE can be found in Boquien et al. (2019).

We model the observed galaxy SEDs with the following components: stellar emission, nebular lines from ionized gas,

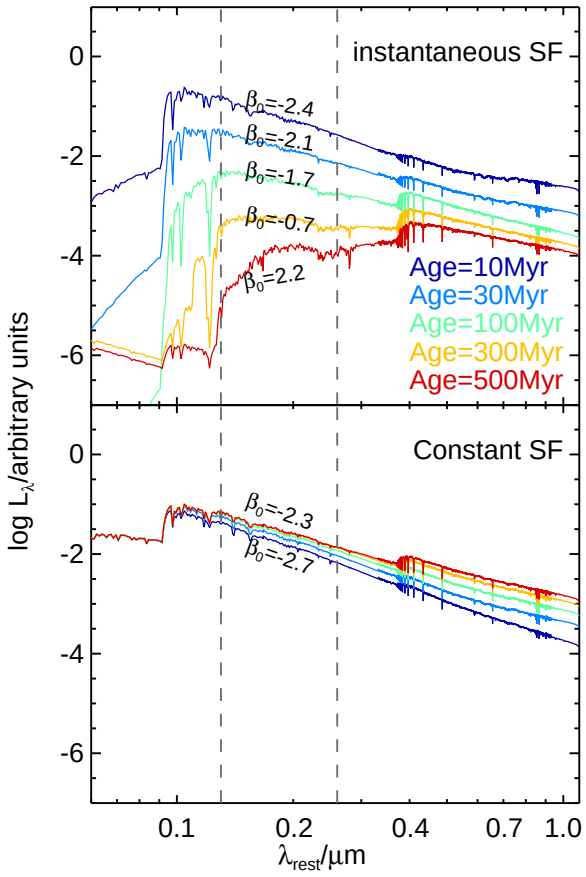


Figure 2. Top: The intrinsic SEDs of galaxy stellar populations from an instantaneous star formation at the ages of $10-500$ Myr for solar metallicity. The UV slope β_0, defined as $L_\lambda \propto \lambda^{\beta_0}$ in the UV, is labelled for each SED. The two dashed lines mark the wavelength range for determining the UV slope. Bottom: Similar to the top panel but for a constant star formation.

[5] https://CIGALE.lam.fr
[6] $\overline{X} = \sum_i (X_i P_i) / \sum_i P_i$

dust attenuation and dust emission. Here the AGN component is not taken into account because our sample contains only SFGs. Following Salim et al. (2018) and Decleir et al. (2019), we fit the UV-to-NIR part of an observed SED, and meanwhile, total IR luminosity derived from observed IR data points is taken as an additional IR 'data point' to balance the dust absorption. The determination of the total IR luminosity is described in Section 2.1.

3.1 Star formation histories

To build a stellar composition, we use the BC03 stellar population synthesis models (Bruzual & Charlot 2003) with a Chabrier (2003) initial mass function. The BC03 models are made with six stellar metallicities. We use four of them from 0.2 to 2.5 $Z_{\odot}$, which is adequate for most galaxies in the local universe (Gallazzi et al. 2005). Following Salim et al. (2016, 2018), we use the two-component exponential models (sfh2exp) offered by CIGALE to set SFHs. It consists of an exponential main (old) component and a recent exponential starburst. Both components are parameterized by the age (t) and e-folding time (τ). The age of the main component ($t_{\rm main}$) is fixed at 11 Gyr, and the e-folding time ($\tau_{\rm main}$) varies from 3 to 11 Gyr in a step of 2 Gyr. The choice of a fixed old stellar age of the main component is to avoid the potential risk of returning unrealistic young stellar ages in the fitting(e.g., Salim et al. 2016, 2018; Decleir et al. 2019; Boquien et al. 2019; Nersesian et al. 2019).

For the starburst component, we notice that a starburst with constant star formation was often adopted in previous studies (Buat et al. 2011a; Salim et al. 2018; Salim & Boquien 2019; Decleir et al. 2019; Salim & Narayanan 2020). The constant starburst is considered as a convenient approximation in SED modelling, but it has a drawback in generating templates with representative intrinsic UV colours (no dust). Koprowski et al. (2020) showed that a constant starburst creates spectral templates of different ages with similar intrinsic UV colours, being less sensitive to the life time of the burst (see also Calzetti 2001; Mao et al. 2012). In Figure 2 we compare the spectral templates in two extreme cases: one an instantaneous starburst (or a single stellar population) and the other a constant starburst. The intrinsic UV slope β_0, defined as the index in the power-law relationship $L_\lambda \propto \lambda^{\beta_0}$ in UV, is measured for each of the intrinsic SED template (no dust) following the methodology of Calzetti et al. (1994). Here metallicity is fixed to Solar. One can see that by increasing age over $10 - 500$ Myr, β_0 changes dramatically from -2.4 to 2.2 for the instantaneous starburst, while β_0 mildly increases from -2.7 to -2.3 for the constant starburst. This is because the galaxy population is constantly replenished by the youngest stellar populations that dominate the UV radiation and result in an approximately constant UV colour (Koprowski et al. 2020; Calzetti et al. 2021).

For our two-component SFH prescription, the UV colour is decided by not only the starburst component but also (partially) the main component. To model the intrinsic SED of a galaxy, we let the age of the starburst ($t_{\rm burst}$) vary from 100 Myr to 500 Myr in a step of 50 Myr. We set up two types of starbursts, having an e-folding time ($\tau_{\rm burst}$) of 100 Myr (declining) and 10 Gyr (constant). The mass fraction of the starburst component varies from 1 to 50 per cent. Combined together, 2376 SED models were generated with different SFHs at each fixed $\tau_{\rm burst}$. The modules and input parameters used to generate model SEDs with CIGALE are presented in Table 1. We also include nebular emission in estimating UV slope, being consistent with the settings in our SED fitting. More details of modelling nebular emission are described in Section 3.3.

Figure 3 shows β_0 as a function of sSFR for model SEDs generated with the two types of starbursts. We can see that both starburst settings produce a reasonable range of sSFR for local SFGs (Guo et al. 2015). We find that β_0 decreases with sSFR, suggesting that younger stellar populations have bluer SEDs in the UV. At given sSFR β_0 increases with stellar metallicity, saying that metal-rich galaxies have higher β_0 (i.e. redder UV colour). The intrinsic linkage between β_0, sSFR, and metallicity is consistent with that in Salim & Boquien (2019). For a constant starburst, the β_0 of the generated model SEDs spread over a small range at $< -2.5\beta_0 < -2.2$ for all four metallicities; For a declining starburst, the model SEDs spread over a wide range of $-2.5 < \beta_0 < -1.3$. This difference of model spreads between the left and right panels is consistent with that given in Figure 2. Again, the constant starburst keeps the UV colour of model SEDs barely changed. Meanwhile, the declining starburst allows a significant fraction of intermediate-age stellar populations to create model SEDs with redder UV colours.

Accumulating evidence from both the observational and theoretical sides shows that galaxies are characterized by bursty and episodic SFHs governed by non-smoothing processes (e.g. Sparre et al. 2017; Iyer et al. 2020). The bursty SFHs cause the intrinsic UV slope (β_0) of the stellar populations to vary over a wide range (e.g. Boquien et al. 2012; Battisti et al. 2016; Schulz et al. 2020; Calzetti et al. 2021). This will be further discussed in Section 6.1. Considering that the dust attenuation (curve) is most sensitive to the UV radiation (Draine 2003; Galliano et al. 2018; Narayanan et al. 2018; Butler & Salim 2021), a steep slope $\beta_0 < -2.2$ for all model SED templates will bias the dust attenuation curve estimated from SED fitting. For example, fitting the observed data with model SEDs of a bluer intrinsic UV colour will result in a steeper attenuation curve according to the degeneracy between SFHs and attenuation curves (Calzetti et al. 2021). In our SED fitting, we take the model SEDs with SFHs of a declining starburst ($\tau_{\rm burst} = 100$ Myr) to conduct our fiducial 'declining starburst fit', as it scans a reasonably wide range of β_0. For comparison, we also perform SED fitting using model SEDs with SFHs of a constant starburst (i.e. $\tau_{\rm burst} = 10$ Gyr) but keep other parameters unchanged. The results are referred to as 'constant starburst fit'. The configurations for the two fittings are listed in Table 1.

3.2 Dust attenuation laws

We adopt the modified Calzetti et al. (2000) Law to describe the dust attenuation curve. Specifically, modifying the Calzetti et al. (2000) attenuation curve with a slope deviation and the 2175 Å absorption feature (Noll et al. 2009) as

$$A(\lambda) = \mathrm{E(B-V)}\left[k(\lambda)\left(\frac{\lambda}{\lambda_{\rm V}}\right)^{\delta} + D(\lambda)\right], \quad (8)$$

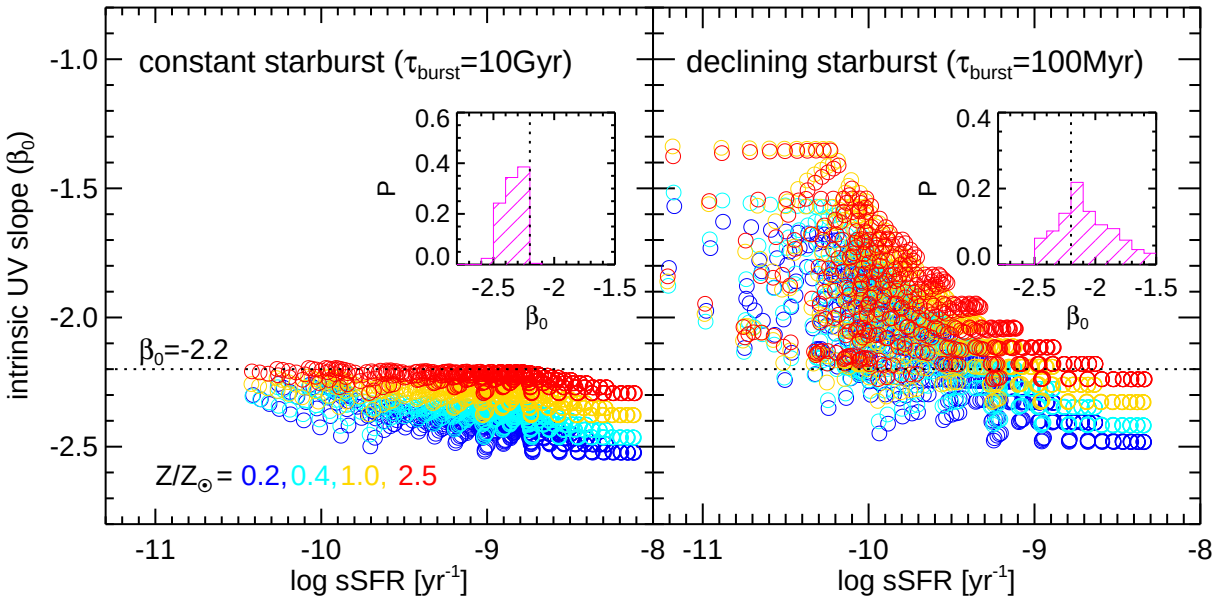


Figure 3. The intrinsic UV slope β_0 as a function of sSFR for our model SEDs. The models are generated with two starburst settings: one is a starburst of constant star formation (left) and the other is a declining starburst (right). The symbols are colour-coded with stellar metallicity 0.2 (blue), 0.4 (cyan), 1.0 (gold), and 2.5 (red) times $Z_\odot$. Note that β_0 decreases with sSFR and increases with metallicity. The dotted lines in both panels mark $\beta_0 = -2.2$. The inner panels show the β_0 histogram of our model SEDs. The vertical dotted lines mark $\beta_0 = -2.2$.

Table 1. Modules and input parameters with CIGALE for generating our model galaxy SEDs. The two configurations have different $\tau_{\rm burst}$.

Module	Parameter	Value
`sfh2exp`	`age_main` (Myr)	11000
	`tau_main` (Myr)	3000, 5000, 7000, 9000, 11000
	`age_burst` (Myr)	100, 150, 200, 250, 300, 350, 400, 450, 500
	`tau_burst`	I. 100 Myr (fiducial declining starburst fit)
		II. 10 Gyr (constant starburst fit)
	`f_burst`	0.01, 0.05, 0.10, 0.15, 0.20, 0.25, 0.30, 0.35, 0.40, 0.45, 0.50
`bc03`	`imf`	1 (Chabrier)
	`metallicity`	0.004, 0.008, 0.02, 0.05
`nebular`	`logU`	−3.0
	`f_esc`	0.0
	`f_dust`	0.0
	`lines_width` (km s^{-1})	300
`dustatt_modified_starburst`	`E_BV_lines`(mag)	0.10, 0.15, 0.20, 0.25, 0.30, 0.35, 0.40, 0.45, 0.50, 0.55, 0.60, 0.65, 0.70, 0.75, 0.80
	`E_BV_factor`	0.44
	`uv_bump_amplitude`	0 (no bump)
	`powerlaw_slope`	−1.4, −1.2, −1.0, −0.8, −0.6, −0.4, −0.2, 0.0, 0.2, 0.4, 0.6
	`Ext_law_emission_lines`	1 (Milky Way)
	`Rv`	3.1
`dale2014`	`alpha`	2.0
	`f_AGN`	0

where $\lambda_V = 0.55\,\mu$m, E(B−V) is the colour excess defined as E(B−V)$\equiv A_B - A_V$, $k(\lambda)$ is the Calzetti et al. (2000) attenuation curve normalized on E(B−V), δ is the deviate power-law slope, and $D(\lambda)$ is the 2175 Å absorption bump (or UV bump). If $\delta = 0$ and no bump is included, Eq. 8 reverts backs to the original Calzetti attenuation curve; and for the Milky Way, it roughly corresponds to $\delta \approx 0.15$ with a bump strength E_b (normalization of $D(\lambda)$) of ≈ 3. Constraining the strength of the 2175 Å bump requires multiple-band photometry or spectroscopy in the UV (e.g. Calzetti et al. 1994; Buat et al. 2011b; Kriek & Conroy 2013; Decleir et al. 2019; Kashino et al. 2021). There are only two broad UV bands included in our dataset and the bump is thus poorly constrained (see also Salim et al. 2018). Here we fix $E_b = 0$, i.e. no 2175 Å bump. We stress that setting the 2175 Å bump as a free parameter or fixing it do not alter our conclusions. CIGALE allows us to separate the young and old stellar populations. The young stellar populations are mostly in the star-forming regions and the old populations are mostly mixed with the diffuse ISM. The former suffers higher attenuation than the latter (Calzetti et al. 1994; Charlot & Fall 2000; Wild et al. 2011; Qin et al. 2019b; Lin & Kong 2020; Li et al. 2021). Calzetti et al. (1994) found that stellar continuum and nebular lines exhibit a different degree of dust attenuation, giving an E(B−V) ratio of ∼0.44 on average. We adopt this value in our SED fitting and use the age of 10 Myr as the boundary to distinguish young and old stars. Here both old and young stellar populations share the same attenuation law but have different E(B−V).

3.3 The nebular emission lines

CIGALE is able to deal with ionized gas radiation (i.e. emission lines) in the model, which has a moderate effect on broadband fluxes and colours of galaxies(e.g., Salim et al. 2016; Yuan et al. 2019). We found that the inclusion of emission lines will moderately increase the quality of SED fitting (decreases of reduced χ^2). Here we use the Inoue (2011) ionized gas radiation model to simulate the emission lines in galaxies. The model is based on CLOUDY 13.01(Ferland et al. 1998, 2013). Following Boquien et al. (2019), we set the ionization parameter to $\log U = -3.0$ and the fraction of Lyman continuum photons absorbed by dust to $f_{dust} = 0$. We find that using a larger or smaller value has no effect on the conclusions. These emission lines are attenuated with a fixed Milky Way extinction curve, while their E(B−V) is consistent with that of young stars.

All the modules and parameters are summarized in Table 1. Combined all possible values for all parameters, a total of 392 040 sub-models are generated for each redshift increased by 0.01 over the sample redshift range. CIGALE is run under two configurations: the fiducial 'declining starburst fit' and the 'constant starburst fit'. The latter is set to be consistent with previous studies, including S20. The main difference between the two configurations is the β_0 coverage (see Figure 3). We show the results of the fiducial declining starburst fit in Section 4 and then show the results of the constant starburst fit for comparison in Section 5.

4 RESULTS FROM THE FIDUCIAL DECLINING STARBURST FIT

We show in this section the results of fitting the observed SEDs of local SFGs with CIGALE for our fiducial declining starburst fit. We firstly examine the possible degeneracies of output parameters, including A_{FUV}, A_V, δ, and β_0 in Section 4.1. We then show the dependence of best-fitting δ on A_V (and A_{FUV}) of our sample galaxies in Section 4.2. Finally, in Section 4.3 we evaluate the effect of fitting degeneracy on A_V–δ relation using simulated data.

4.1 The degeneracies of β_0, δ, A_V, and A_{FUV} in SED fitting

The Bayesian approach can be used to examine the robustness of the output parameters with the probability distribution function (PDF) (Han & Han 2014; Sharma 2017; Boquien et al. 2019; Yuan et al. 2019). Degeneracies between parameters can be seen by correlations in posterior probability distributions (Leja et al. 2017; Hagen et al. 2017; Han & Han 2019; Doore et al. 2021). Figure 4 shows the probability distribution for galaxy parameters β_0, δ, A_V, and A_{FUV}, for a typical galaxy with the best-fitting galaxy parameters and errors representative among the sample.

From panel (g) of Figure 4 one can see that δ is degenerate with the intrinsic UV slope β_0 in the sense that a lower β_0 (bluer in the UV) is coupled with a smaller δ (steeper attenuation curve). The Spearman's rank correlation coefficient ρ_s between the two parameters is ∼0.66. The SED of a young stellar population attenuated by a given dust attenuation curve can be replaced with the SED of an older stellar population attenuated by a flatter attenuation curve. This is the well-known degeneracy between stellar population age and the steepness of the dust attenuation curve (Hagen et al. 2017; Calzetti et al. 2021). In the framework of SED fitting based on the energy balance approach, the IR luminosity is used to constrain the integrated energy that is absorbed by dust; but how the energy is absorbed across wavelength, i.e. the attenuation curve, is not constrained. Therefore the traditional method of SED fitting is not able to break this β_0–δ degeneracy effectively. Both β_0 and δ are poorly constrained in our SED fitting with CIGALE.

Panel (h) of Figure 4 shows a strong degeneracy between δ and A_V ($\rho_s = 0.84$). The higher A_V, the flatter the attenuation curve. A similar trend is also presented in Hagen et al. (2017) and S20. This degeneracy is probably responsible for the well-established relation between A_V and the attenuation curve slope δ (Salmon et al. 2016; Salim et al. 2018; Salim & Narayanan 2020; Battisti et al. 2020). We find that A_V is weakly degenerate with β_0 ($\rho_s = 0.36$), in the sense that a higher A_V is seen at a higher β_0 (redder in the UV). Combined together, the three parameters A_V, δ, and β_0 seem to be degenerate with each other. This can be easily verified with the relation between two parameters by fixing the third one. As shown in the top-right panels of Figure 4, when we fix one parameter of the three, the degeneracy between the other two is to some extend compressed. For example [the panel (k)], the $1\,\sigma$ dynamical range of β_0 ($\log A_V$) decreases from ∼0.5 (∼0.5) to ∼0.3 (∼0.2) if we fix $\delta = -0.2$. These results support that the three parameters A_V, δ, and β_0 are degenerate with each other. This is to say that a redder intrinsic SED, a higher A_V or a lower δ (steeper attenuation

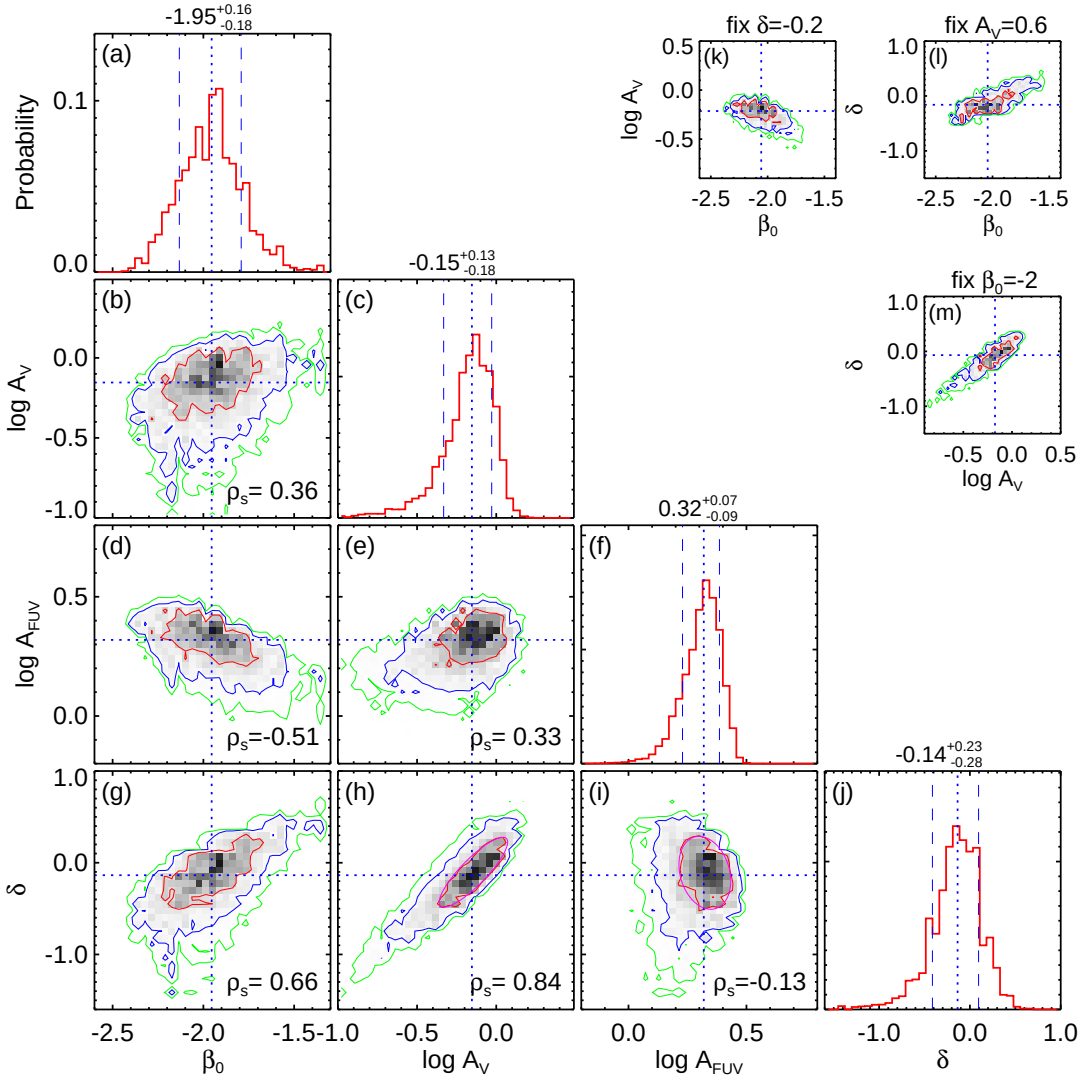


Figure 4. The posterior probability distributions of β_0, A_V, A_{FUV}, and δ from our SED fitting of a typical galaxy. Here the declining starburst is adopted in building SFHs and model SEDs. In each panel, the blue dotted lines mark the 50th percentile values (slightly differ from the likelihood-weighted mean values). In each histogram plot, the 16th and 84th percentiles are marked with the dashed lines. The red, blue and green contours enclose 68, 95, and 99 per cent of probability (i.e. 1, 2, and 3 σ), respectively. The magenta ellipses in panels (h) and (i) best fit the 1 σ contours. The Spearman's rank correlation coefficient ρ_s is also presented in each panel. The top-right three panels (k, l, and m) show the probability distributions if fixing one parameter.

curve) in SED fitting may end up with similar model SEDs matching an observed SED. We refer it to as the A_V–δ–β_0 degeneracy.

Moreover, we notice that FUV attenuation (A_{FUV}) does not feature a strong degeneracy with δ ($\rho_s = -0.13$) as shown in panel (i). The ratio of A_{FUV} and A_V (A_{FUV}/A_V) represents the attenuation curve slope. Figure 4 shows that the presence of strong A_V–δ but no A_{FUV}–δ degeneracy indicates that the variation of dust attenuation curve slope in SED fitting is mostly driven by the change of A_V instead of A_{FUV}. This is not surprising since the energy absorbed by dust comes mostly from the UV rather than the optical (Cortese et al. 2008; Kennicutt & Evans 2012). If there is a fluctuation in δ in the SED fitting (coming from the β_0–δ degeneracy), a consequent change in A_V is more preferred than in A_{FUV}, because changing A_V have less effect on energy balance than chaning A_{FUV}. As a consequence, the typical scatter of log A_V is systematically larger than that of log A_{FUV} (0.16 vs 0.08). The extra contribution comes from the scatter of δ. The fluctuations in log A_V and δ are highly degenerate and can bias the A_V–δ relation derived from SED fitting.

To address these fitting degeneracies more clearly, we show the PDFs between A_V and δ across the A_V–δ plane of our sample of 2 291 galaxies (the background contour) in Figure 5. We find that the A_V–δ degeneracy is not monochromatic across the A_V–δ plane of our sample galaxies. The scope of degeneracy decreases with A_V, and at a fixed A_V, it decreases mildly with δ. Despite the amplitude changing dramatically across the A_V–δ plane, the degeneracy fluctuations in log A_V and δ change in a lock step (with a slope of ∼2). The top-left panel shows the dependence of the uncertainties of δ and log A_V on log A_V for our sample galaxies. The uncertainties of both δ and log A_V decrease with log A_V. The uncertainty in δ is about a factor of 2 times that in log A_V.

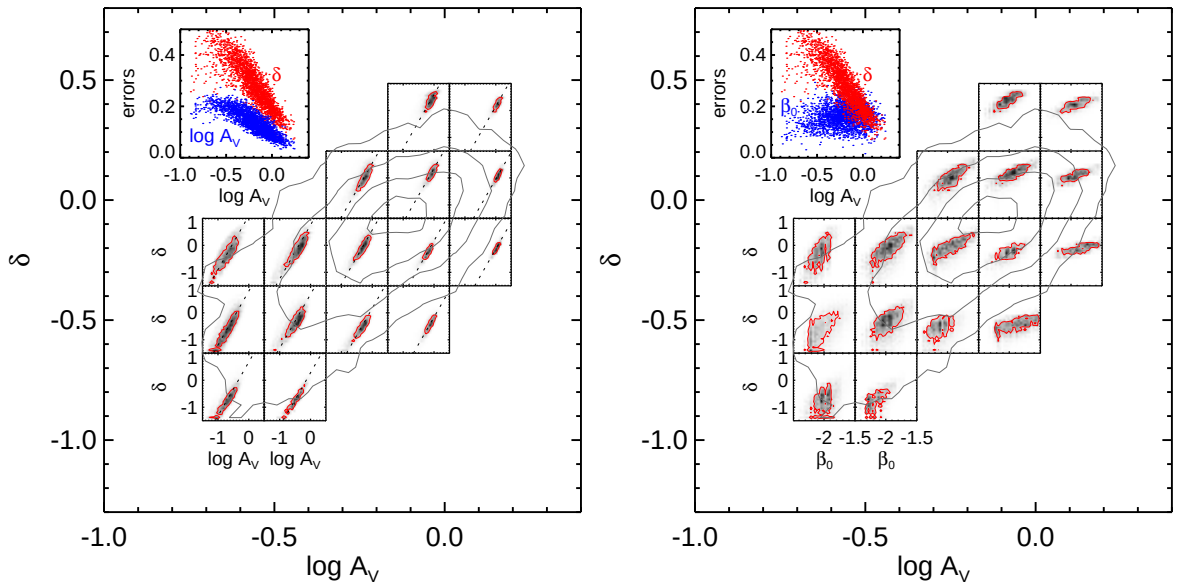


Figure 5. Left: Background contours show the distribution of sample galaxies in the A_V–δ plane. The inner grid panels show the PDFs between A_V and δ for galaxies at that location in the A_V–δ plane. In each inner grid panel, red contour marks the 1 σ-level of PDF, and the dotted line has a slope of 2 and passes through the median value. The small panel in the top-left corner shows the errors of δ (red) and A_V (blue) as a function of A_V for our sample of 2 291 SFGs. Right: Similar to the left plot but showing PDFs between β_0 and δ. The top-left small panel shows the errors of δ (red) and β_0 (blue) as a function of A_V for our sample galaxies.

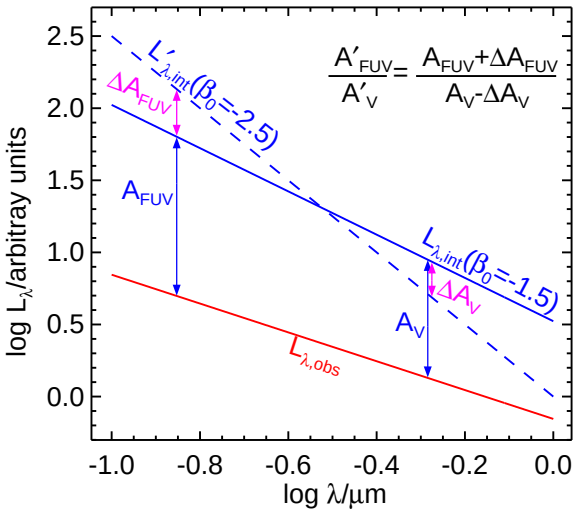


Figure 6. Schematic diagram of the influence of β_0 fluctuation on attenuation curve slope in the SED fitting based on the energy balance principle. Two intrinsic SEDs have the same bolometric luminosity but have different UV slopes ($\beta_0 = -2.5$ and -1.5). The two UV slopes are roughly chosen as the dynamic range boundaries for model SEDs, and $\Delta A_{\rm FUV}$ and ΔA_V represent the maximum variation of dust attenuation caused by β_0 fluctuation. By definition, the amount of attenuation ($A_{\rm FUV}$, A_V, $\Delta A_{\rm FUV}$, and ΔA_V) is proportional to the length of respective arrows given in the plot, i.e. $A_\lambda = -2.5\log(L_{\lambda,\rm obs}/L_{\lambda,\rm int}) \propto \log L_{\lambda,\rm int} - \log L_{\lambda,\rm obs}$. The relationship between the two attenuation curve slopes (parameterized by $A_{\rm FUV}/A_V$) is also given.

It can be understood that the measurement uncertainty in δ exhibits a dependence on $\log A_V$. Figure 6 illustrates how a change in β_0 affects the determination of the attenuation curve slope δ in SED fitting. As discussed above, the uncertainties in δ in part originate from the variation in β_0. There are two ways to result in a smaller uncertainty for the attenuation curve slope δ. One is to reduce the dynamical range of β_0 for model SEDs used in the SED fitting. We will show in Section 5 that a constant starburst setting with a narrow range of β_0 leaves on average a smaller uncertainty in δ [see also in the panel (m) of Figure 4]. Here for a given fitting configuration, the dynamical range of β_0 is fixed, and the uncertainties in β_0 is more or less constant (see in the right panel of Figure 5). The second way is to increase the global dust attenuation (both $A_{\rm FUV}$ and A_V). As shown in Figure 6, for a certain SED fitting, the maximum variation of dust attenuation (e.g. $\Delta A_{\rm FUV}$ and ΔA_V) caused by the change in β_0 is strictly limited. With the increase in global dust attenuation, both the $\Delta A_{\rm FUV}$ and ΔA_V become less significant relative to the large $A_{\rm FUV}$ and A_V. As a consequence, the attenuation curve slope δ will be decreasingly affected by the change in β_0. It is clear that the β_0–δ degeneracy is almost gone at the high end of A_V, as shown in Figure 5 (the right panel). Although the scatter of β_0 remains large at high A_V, the uncertainty in δ drop significantly. This effect of 'decreasing influence of β_0 on δ at higher A_V' is also the key to understanding the different fitting results from our two fit configurations. We will come back to this in Section 5.2.

4.2 The correlation between δ and A_V estimated with CIGALE

Figure 7 shows our results from the CIGALE SED fitting of the observed SEDs for our sample of 2 291 local SFGs. The relation between attenuation curve slope δ and dust attenuation A_V is clearly seen. At increasing A_V, the dust attenuation curve becomes flatter with increasing δ. We compare our

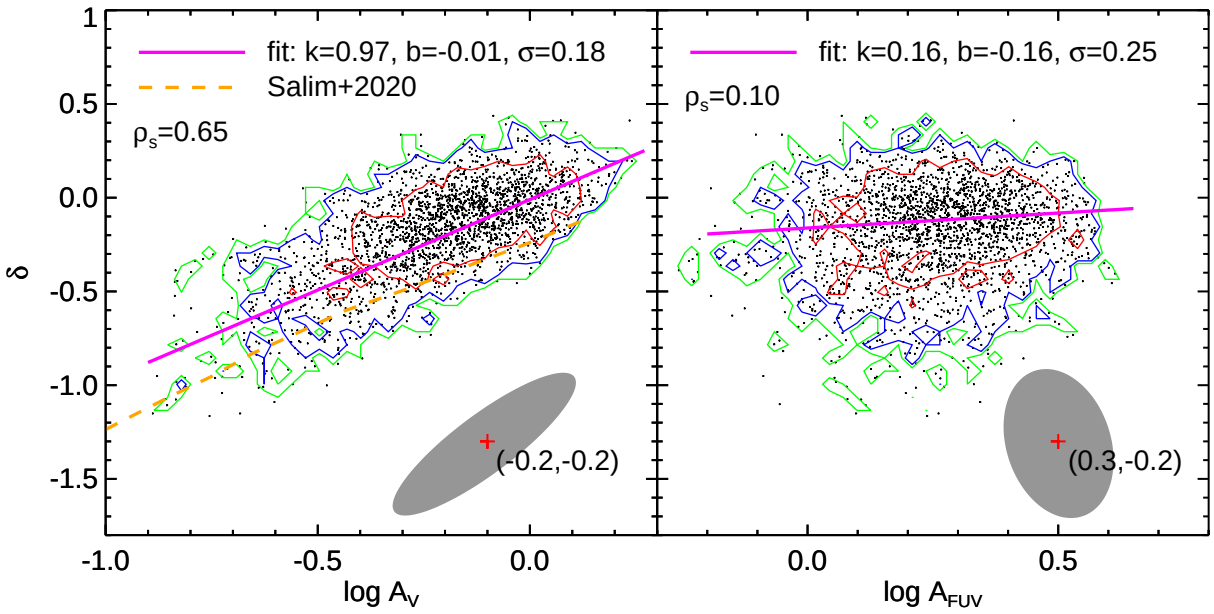


Figure 7. Left: Attenuation curve slope δ as a function of A_V on the basis of best fits with CIGALE under the fiducial declining starburst setting for our sample of 2 291 local SFGs. The red, blue, and green contours enclose 68, 95, and 99 per cent of sample galaxies, i.e. 1, 2, and 3 σ, respectively. The magenta solid line is the relation best fitting the data points. The best-fitting parameters ($Y = k \times X + b$) and dispersion (σ) are also presented. The orange dashed line represents the median relation given in S20. The Spearman's rank correlation coefficient (ρ_s) between A_V and δ is also labelled. The error ellipse at the bottom-right corner represents the 1 σ degeneracy error of the typical galaxy taken from Figure 4. The A_V and δ of this typical galaxy are marked. Right: Similar to the left plot but showing the relation between δ and A_{FUV}.

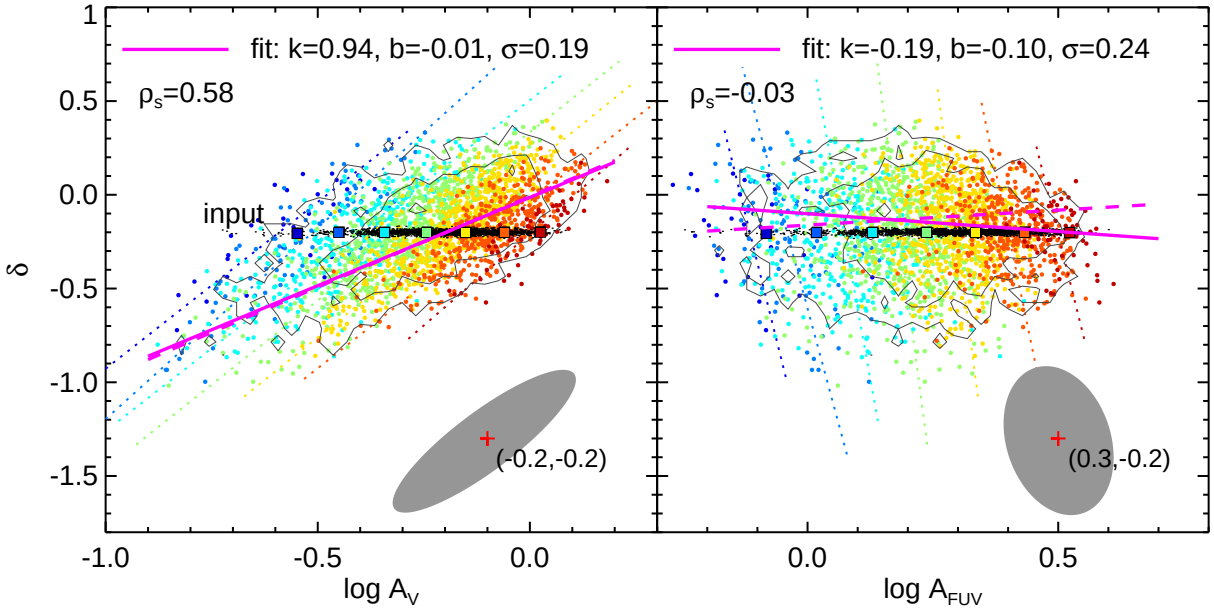


Figure 8. Left: The best-fitting δ as a function of A_V for the simulated galaxies. The blue-to-red colour indicates increasing values of the input A_V. The two contours enclose 68 and 95 per cent data points. The black points are the input flat A_V–δ relation with a fixed δ of −0.2. These data are slightly scattered in δ for demonstration. The coloured squares are the median of black points divided into different input A_V bins. The dotted lines are the best-fitting relations of simulated galaxies in different input A_V bins. The magenta solid line represents the relation best-fitting the sample. The best-fitting parameters and associated scatter are given in the legend. The magenta dashed line is the best-fitting relationship taken from Figure 7. The Spearman's rank correlation coefficient (ρ_s) between A_V and δ is also labelled. The error ellipse in bottom-right represents the typical degeneracy error. Right: Similar to the left but showing the relation between δ and A_{FUV}.

A_V–δ relation to that given in S20.[7] We find that our A_V–δ relation is consistent with S20's but systematically higher in δ (shallower attenuation curve). The discrepancy is attributed to the adoption of a constant starburst for model SEDs in S20 (see in Section 5).

We show the typical degeneracy error in the form of an error ellipse for comparison. The error is defined as the $1\,\sigma$ posterior distribution between δ and A_V (see in Figure 4). It is clear that the size of the error ellipse between δ and A_V appears comparable to the distribution of our sample galaxies (the $1\,\sigma$ red contour). We remind that the global dispersion of δ ($\sim$0.25) is slightly lower than the median uncertainty of δ ($\sim$0.28), indicating that the scatter in δ for our sample SFGs mainly come from the fitting uncertainties. The $1\,\sigma$ dispersion around the best-fitting relation is $\sim$0.18, which is significantly smaller than the uncertainty of δ. Generally speaking, the dispersion around the best-fitting relation is unlikely lower than the fitting uncertainty. However, this statement only holds when the two errors are independent. If the errors of two variables are correlated with each other, like our A_V and δ, it will strengthen the correlation and leave the dispersion smaller than the measurement errors.

On the other hand, the local SFGs in our sample show no correlation between A_{FUV} and δ, as shown in the right plot of Figure 7. The independent error ellipse further confirms the robustness of this flat relation. Considering the large scatter in δ, a flat A_{FUV}–δ relation does not conflict with a positively-correlated A_V–δ relation. We notice that the A_V–δ relation is significantly biased by the fitting degeneracy (even comparable). It gives rise to a possibility that the 'true' δ does not correlate with either A_V or A_{FUV} ($\sim$ dust column density; Butler & Salim 2021), while the measured A_V–δ relation comes from the fitting degeneracy.

4.3 A simulation test with a flat A_V–δ relation

We conduct a simulation test to verify the possibility of lacking intrinsic dependence of attenuation curve slope on A_V. We carry out the simulation by setting the 'true' attenuation slope unchanged with A_V, and testing if the fitting degeneracies produce a similar A_V–δ relation? To do so, we firstly create a set of mock galaxy SEDs satisfying a flat A_V–δ relation, i.e. a fixed δ over a range of A_V, and then perform the same SED fitting to the mock data.

We generate mock galaxy SEDs as follows. From the best-fitting results of Figure 7, we use the recovered intrinsic SEDs of our sample galaxies and attenuate them by the corresponding A_{FUV} with the dust attenuation curve of fixed $\delta = -0.2$. The best-fitting A_{FUV} is adopted since it better traces dust attenuation than A_V (see Figure 4). Taking into account the fitting uncertainties, here the dynamical range of input A_{FUV} slightly shrinks by $\sim$15 per cent. The value of $\delta = -0.2$ roughly corresponds to the median value of our sample SFGs. We calculate fluxes in all bands and assign them errors the same as the measurement errors relative to the observed fluxes. As mentioned in Section 3.1, about 10 per cent uncertainties are added to the band fluxes in CIGALE, to account for the uncertainties from the models themselves. To be consistent, the additional 10 per cent model errors are also included in generating mock SEDs. The attenuated fluxes are added with deviations randomly given by a normal distribution with the assigned errors as the dispersion. IR luminosity is calculated by integrating the total energy attenuated by dust (also adding errors). After that, we obtain simulated galaxy SEDs satisfying a known (flat) A_V–δ relation. The flux distributions in all bands we examined are similar between our mock SEDs and the observed ones. We run CIGALE to repeat the same SED fitting (with δ as a free parameter) to our mock galaxy SEDs, and determine the best-fitting attenuation parameters.

Figure 8 shows the derived δ as a function of A_V from our fitting of the mock galaxy SEDs. We find the distribution of best-fitting δ appears similar to that in Figure 7 even though the input δ is fixed to -0.2 (the black points). This indicates that the variations in δ for our sample SFGs mainly come from the fitting uncertainties. Compared with the input values, the output δ and A_V deviate following the degeneracy error with a slope of $\sim$2. The deviations are larger at lower input A_V (with bluer colour), consistent with the increasing degeneracy error at decreasing A_V shown in Figure 5. The degeneracy error alters the input flat relation and forms an A_V–δ relation similar to the A_V–δ relation reported in the literature. The A_V–δ relation given in Figure 7 is presented by the magenta dashed line for comparison. We can see that the mock-based relation has a slope of 0.94 in comparison with the slope of 0.97 for the dashed line. Not only the best-fitting slopes agree but also the scatter of data points mirror each other: 0.19 and 0.18 for mock- and observation-based relation, respectively. The fitting degeneracies seem to be a dominant driver of the established A_V–δ relation. In addition, the right panel of Figure 8 shows the independent error in A_{FUV} increases the scatter in δ, but does not alter the input flat A_{FUV}–δ relation significantly. Our simulation test confirms that the degeneracy error can significantly bias a flat A_V–δ relation and result in a A_V–δ relation similar to what we often see in the literature. We thus conclude that the strong A_V–δ correlation derived from SED fitting is a false relation governed by fitting degeneracies.

5 FITTING WITH MODEL SEDS OF CONSTANT STARBURST SFHS

Our finding that the A_V–δ relation is dominated by fitting degeneracies disagrees with the result from S20 that the size of degeneracy error is significantly smaller compared to the tight global correlation. As we pointed out, the use of model SEDs made with constant starburst SFHs in their SED fitting is mainly responsible for this difference. We decide to conduct SED fitting in the same way and make a quantitative comparison between the fitting results from the constant starburst and declining starburst settings.

5.1 The outputs from the constant starburst fitting

Following Section 4.1, we show the degeneracies between galaxy attenuation parameters for the same typical galaxy in Figure 9. We stress that β_0 of the model SEDs from the constant starburst SFHs is distributed in a narrow range around

[7] S20 used the UV-optical slope, defined as $S = A_{1500}/A_V$, to parameterize the attenuation curve slope. The conversion follows $\delta = 0.71 - 1.91 \times \log S$ for our sample SFGs.

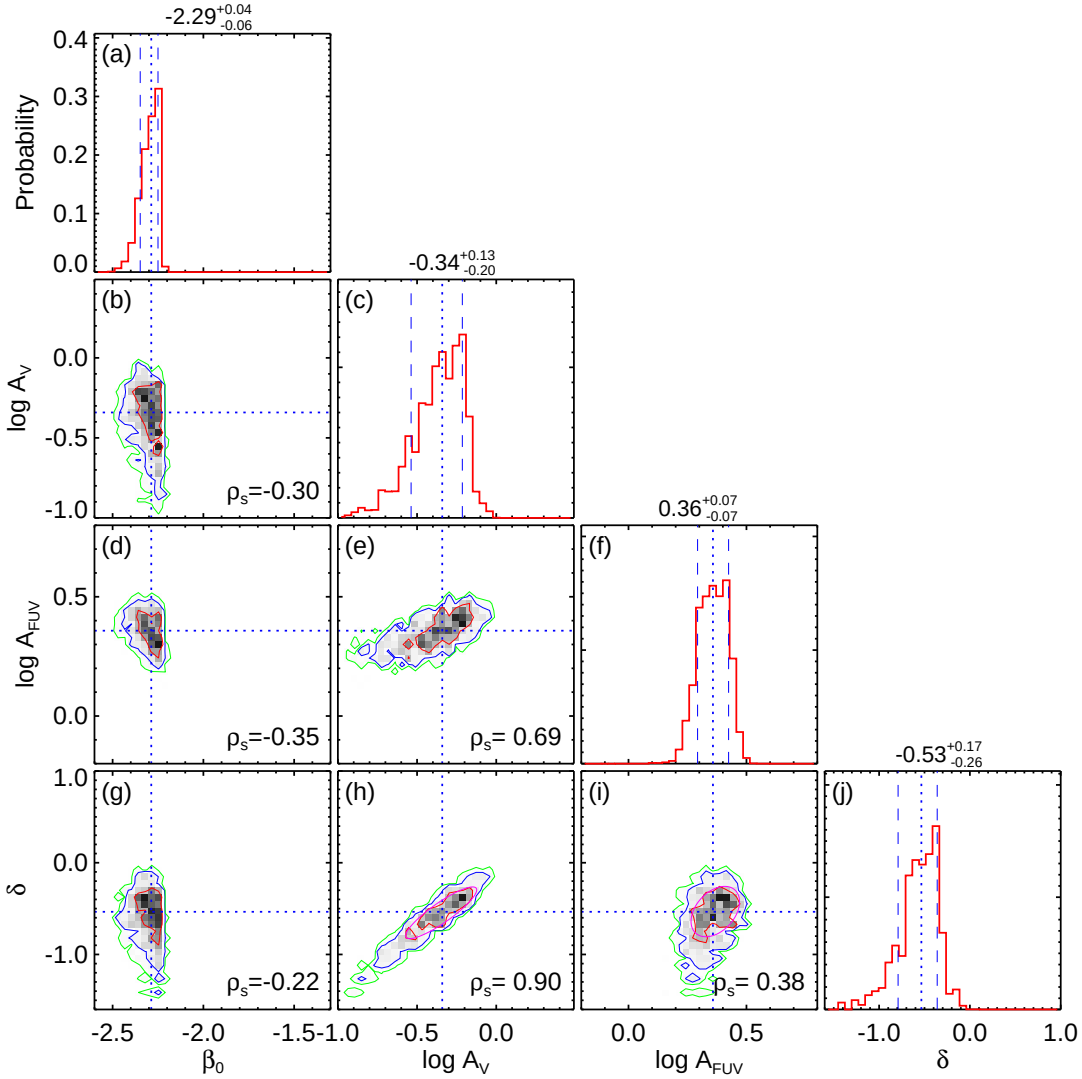


Figure 9. Similar to Figure 4 but showing the results derived using model SEDs with the constant starburst SFHs.

Table 2. Comparison of the median best-fitting parameters and χ^2_r between the declining starburst and constant starburst settings for SED fitting of our local sample.

	β_0	δ	logA_V	logA_{FUV}	χ^2_r
fiducial declining starburst	-2.00±0.16	-0.14±0.28	-0.19±0.14	0.26±0.08	0.18
constant starburst	-2.33±0.05	-0.54±0.22	-0.34±0.13	0.32±0.06	0.28

$\beta_0 = -2.3$ and the degeneracy of β_0 with δ (as well as A_V) is largely compressed. The narrow range of β_0 does not mean that β_0 is well determined. Instead, it is decided by the chosen model SEDs (see Figure 3). In other words, β_0 is not a fully free parameter in the SED fitting with the constant starburst setting. As a consequence, the median error of β_0 (for our sample), calculated as the standard deviation of the PDF, decreases significantly from ∼0.16 for the declining starburst setting to ∼0.05 (see Table 2). As discussed in Section 4.1, a 'well' constrained β_0 will subsequently lead to a smaller error in δ. The median error of δ decreases from ∼0.28 to ∼0.22. Although δ is degenerate with A_V, the degeneracy error is relatively smaller. The median error of δ is moderately larger than the median value of ∼0.17 given in S20 using a similar constant starburst setting.[8] This noticeable difference might be partially due to the dynamical range of $[-1.4, 0.6]$ for δ in our SED fitting slightly larger than the range of $[-1.2, 0.4]$ given in S20. We verify that a smaller typical error of ∼0.20 will be obtained if a consistent δ range is set in our SED fitting.

On the other hand, the limitation of $\beta_0 < -2.2$ in the

[8] S20 conducted the analysis with the same GSWLC-D sample used in Salim & Boquien (2019). More details can be found in the latter work as well as in Salim et al. (2018).

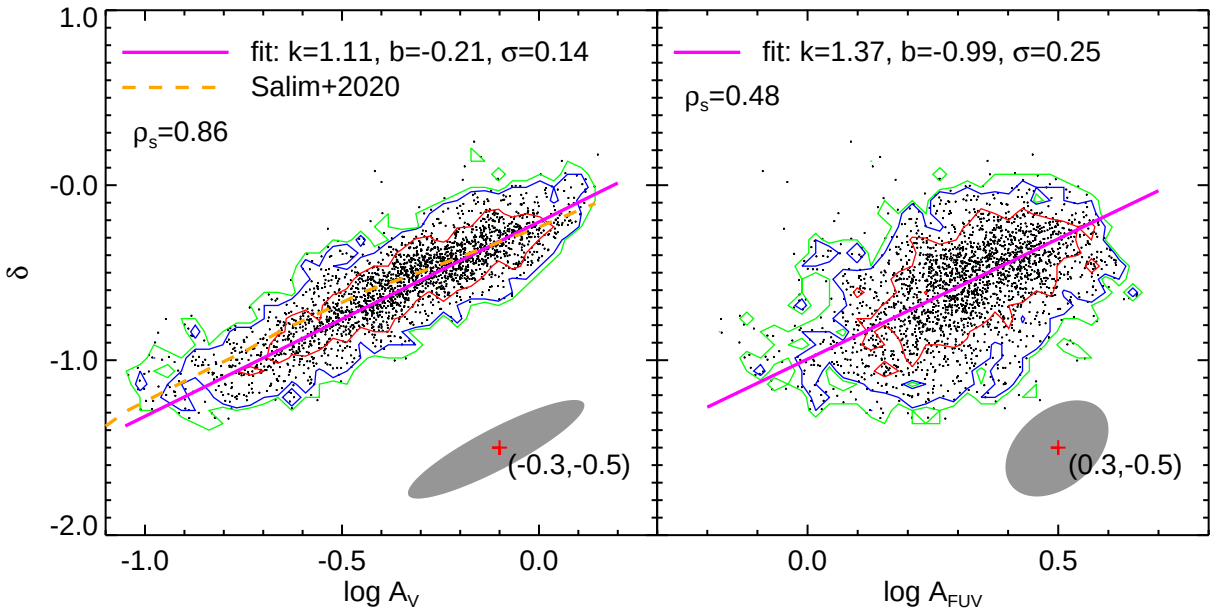


Figure 10. Similar to Figure 7 but showing the results from the fitting with model SEDs of constant starburst SFHs.

constant starburst setting subsequently biases the derived attenuation curves. Table 2 summarizes the median parameters (for our local 2 291 SFGs) and corresponding errors estimated from two sets of SED fitting. One can see that β_0 from the constant starburst fitting is much smaller (bluer intrinsic UV colour) than that of the declining starburst fitting. As a consequence, it returns a steeper attenuation curve according to the β_0–δ degeneracy (see Figure 4). The median of -0.54 for δ from the constant starburst fitting is slightly lower that the median of -0.42 presented in S20. Still, the median attenuation curve is systematically steeper than that from the declining starburst fitting (median is $\delta = -0.14$). Generally speaking, a steeper attenuation curve can be reflected by either an increasing $A_{\rm FUV}$ or decreasing $A_{\rm V}$. From the declining starburst fitting to the constant starburst fitting, the median best-fitting $\log A_{\rm FUV}$ increases by only 0.06 dex while $\log A_{\rm V}$ decreases by 0.15 dex. This is consistent with the expectation that the fluctuation in δ (error-driven) in the energy-balance fitting is more linked with $A_{\rm V}$ than $A_{\rm FUV}$ in Section 4.1.

We notice that the declining starburst fit yields an smaller reduced chi-square $\chi^2_{\rm r}$ than that of a constant starburst fit. Moreover, the two $\chi^2_{\rm r}$ are smaller than unity, indicating either an over-fitting or an overestimate of errors. The latter seems reasonable since, by default, additional 10 per cent model errors are added to the 'input' photometry errors (i.e., overestimate of errors). More importantly, we note that the $\chi^2_{\rm r}$ presented here is defined as $\chi^2/(N-1)$, where N is the number of data points. This differs from the 'true' reduced χ^2 which is defined as $\chi^2/N_{\rm dof}$, where $N_{\rm dof}$ is the number of degrees of freedom (Andrae et al. 2010). The $N_{\rm dof}$ can be estimated for linear models as $N_{\rm dof} = N - K$, where K is the number of free parameters. For the nonlinear models (like our SED-fitting), it is questionable whether it can be accurately calculated (Andrae et al. 2010; Małek et al. 2018). Given that K always greater than 1, the $\chi^2_{\rm r}$ presented here $[\chi^2/(N-1)]$ should be always smaller than the 'true' value of $\chi^2/(N-K)$. We thus do not treat the small $\chi^2_{\rm r}$ outputted by CIGALE as a sign of over-fitting (see also Małek et al. 2018; Nersesian et al. 2019; Boquien et al. 2019; Ren et al. 2022).

Figure 10 shows the $A_{\rm V}$–δ relation from the constant starburst fitting, being in good agreement with the relation from S20. Again we emphasize that the model SEDs with constant starburst SFHs are adopted in both of the two. We point out the degeneracy error is relatively smaller compared to the global $A_{\rm V}$–δ relation, consistent with S20. Compared with the results by the declining starburst fitting, the relation here is tighter and has a smaller dispersion (σ decreases from 0.18 to 0.14). Moreover, the right panel shows the δ as a function of $A_{\rm FUV}$. For the declining starburst fitting, the relation is flat, and for a constant starburst fitting, δ moderately increases with $A_{\rm FUV}$. An additional dependence of δ on $A_{\rm FUV}$ (or global dust attenuation) appears when the constant starburst fitting is applied.

5.2 Understanding the SED fitting results with the declining starburst and constant starburst settings

We have demonstrated that the main difference between the declining starburst and constant starburst settings is the dynamic range of β_0. Unlike the widely distributed β_0 from -2.5 to -1.5 generated by the declining starburst setting, the constant starburst setting scans a very limited range $\beta_0 = [-2.5, -2.2]$. The best-fitting β_0 from the declining starburst runs has a median of $\sim --2$, which is much higher (redder in the UV) than the β_0 coverage in the constant starburst fitting. It is worth noting that local SFGs tend to have high β_0 (red UV colour) and spread in a wide range (more will be discussed in Section 6.1). Then the constant starburst fitting produces inappropriately lower β_0 (bluer UV colour). This underestimate of β_0 will be translated into a smaller δ in SED fitting according to the β_0–δ degeneracy. However, as mentioned in Section 4.1 (Figure 6), the change in δ caused by the deviation of β_0 is dependent on the global dust attenuation. In the low dust attenuation regime, the constant

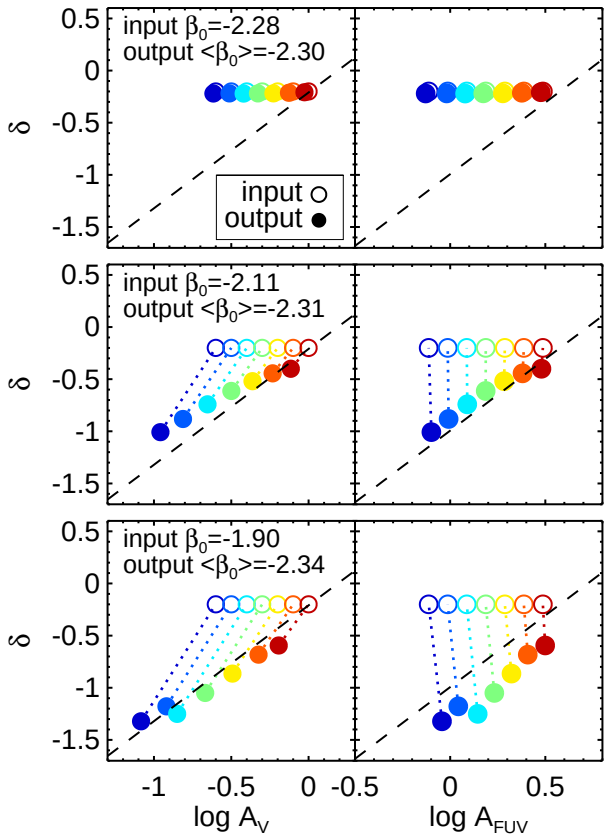


Figure 11. Attenuation curve slope δ as a function of A_V (left) and A_{FUV} (right) estimated from the constant starburst fitting to the simulated galaxy SEDs with a fixed $\beta_0 = -2.28$ (top), -2.11 (middle), and -1.90 (bottom). The open and filled circles represent the input and output attenuation parameters, respectively, connected by dotted lines. The colour-coding reflects input A_V (or A_{FUV}). The dashed lines in these panels refer to the best-fitting relations taken from Figure 10. The average of output β_0 is presented in each left panel.

starburst fitting (with model SEDs bluer in the UV) gives a smaller δ with large deviation; in the high dust attenuation regime (both A_V and A_{FUV}), δ is no longer sensitive to the change in β_0 and has a small deviation. The higher the dust attenuation, the higher the δ. Combined together, these biases and scatters caused by fitting degeneracies induce a positive relation between the attenuation curve slope δ and global dust attenuation (both A_V and A_{FUV}). Moreover, if dust attenuation is extremely high, the selection bias in β_0 no longer affects the derived δ; and the declining starburst and constant starburst two fittings will output similar attenuation curves.

Aiming to further ascertain these effects, we perform SED fitting with the constant starburst setting to mock galaxy SEDs of different 'true' β_0. The intrinsic galaxy SEDs come from the CIGALE SED libraries generated with the declining starburst setting. Considering that β_0, sSFR and metallicity of the model SEDs are correlated with each other (see Figure 3), we pick those with sSFR and metallicity to be representative of our sample SFGs, i.e, with $\log \mathrm{sSFR} \approx -9.6\,\mathrm{yr}^{-1}$ and $Z = Z_\odot$. Here we focus on three model SEDs with $\beta_0 = -2.28$, -2.11, and -1.90. Next step, we attenuate each model SED with the attenuation curve of a fixed slope $\delta = -0.2$ in combination with a set of A_V over $\log A_V = [-0.6, 0]$. We derive the fluxes in all bands involved in our catalogue. IR luminosity is calculated by integrating the total energy attenuated by dust. To better illustrate the artefact of β_0 bias, we do not add any errors (and perturbation) to these band fluxes. With these mock galaxy SEDs, we repeat SED fitting with the constant starburst setting and present the recovery of attenuation parameters in Figure 11.

We remind that the recovered intrinsic UV slope from the constant starburst fitting remains steep ($\beta_0 < -2.2$). For the mock SED of $\beta_0 = -2.28$ (the top-left panel), the SED fitting can well recover the input β_0, δ, and A_V. For the mock SEDs of $\beta_0 = -2.11$ and -1.90 (the middle-left and bottom-left panels), the recovered β_0 (~ -2.3) deviates dramatically from the input value. As a consequence, the recovered δ is increasingly smaller at decreasing $\log A_V$. The deviation becomes increasingly larger for higher β_0 due to the fitting degeneracies between β_0, δ, and A_V. Again, the underestimate of δ is dependent on A_V — the deviation of δ from the input value decreases at increasing A_V. A strong correlation can be seen between the recovered A_V and δ for the two model SEDs of input $\beta_0 > -2.2$. Such correlation also holds for A_{FUV}, as shown in the right panels of Figure 11. It becomes clear that the biases in recovering δ and A_V originate from the fitting degeneracies between β_0, δ, and A_V.

Interestingly, the bottom-left panel of Figure 11 shows the recovered A_V–δ relation (solid circles) following the A_V–δ relation (the dashed line) for our sample of local SFGs presented in Figure 10. One question naturally arises — *do the biases driven by fitting degeneracies fully account for the formation of the observed A_V–δ relation?* We quantitatively evaluate the effects of these biases through SED fitting on the mock galaxy SEDs with a fixed δ of -0.2 presented in Section 4.3. We analyse the systematic biases as examined before. We note that the mock galaxy SEDs span a wide range in β_0, and thus allow to generate biases induced by the β_0-related degeneracies in the SED fitting with the constant starburst setting. We show the fitting results in Figure 12.

One can see that with a fixed input δ for all mock galaxy SEDs, the fitting returns the recovered attenuation parameters forming an A_V–δ relation (both slope and scatter) similar to that derived for our sample of local SFGs (Figure 10). We remind that Figure 12 is for mock galaxy SEDs attenuated by the same dust attenuation curve of $\delta = -0.2$, while Figure 10 is for our sample of 2 291 local SFGs. The SED fitting with the constant starburst setting more or less recovers the input δ at the high end of A_V but increasingly underestimates δ at decreasing A_V. We emphasize that this correlation between the recovered A_V and δ in Figure 12 is completely attributed to the systematic biases induced by degeneracy errors between δ, A_V, and β_0 in the SED fitting with the constant starburst setting.

The right panel of Figure 12 shows that a correlation of δ with A_{FUV} is also recovered. This A_{FUV}–δ correlation is mainly due to the bias of constant starburst setting that the intrinsic UV slope of all model SED templates is set to $\beta_0 < -2.2$. When the model SED templates span over a wide range of β_0 as given by the declining starburst setting, the recovered δ no longer depends on A_{FUV} (the right panel of Figure 8). Our simulation results explain why S20 delivered a tight A_V–δ relation with smaller degeneracy errors (under the constant starburst setting). We conclude that the degenera-

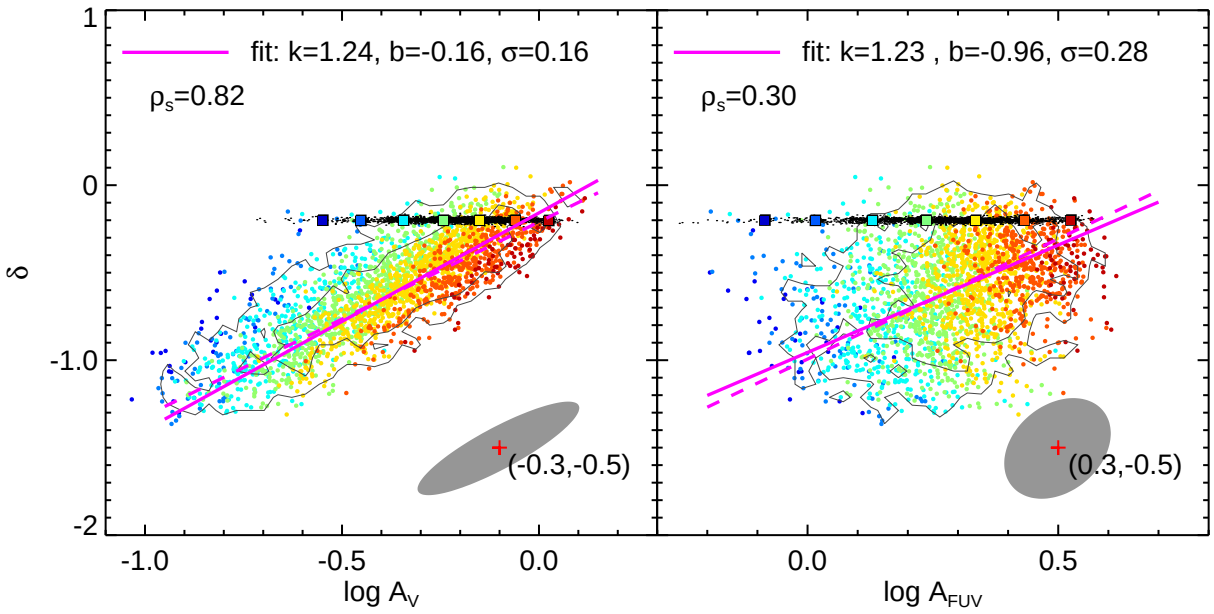


Figure 12. Similar to Figure 8, but the SED fitting is done with the constant starburst setting. The magenta dashed lines refer to the best-fitting relations from Figure 10.

cies between dust attenuation curve slope δ, dust attenuation $A_{\rm V}$, and the intrinsic UV slope of model galaxy SEDs β_0 in SED fitting cause systematic biases in deriving these quantities and result in false correlations between $A_{\rm V}$ ($A_{\rm FUV}$) and δ.

6 DISCUSSION

6.1 Distribution of the intrinsic UV slope among local SFGs

A well-designed declining starburst SFH is introduced in this work to generate model SEDs for fitting the observed galaxy SEDs, in comparison with the constant starburst SFH often adopted in previous studies (Giovannoli et al. 2011; Buat et al. 2012; Salim et al. 2016; Małek et al. 2018; Salim et al. 2018; Salim & Boquien 2019; Salim & Narayanan 2020). The model SED templates from the constant starburst SFHs have the intrinsic UV slope (β_0) in a limited range of $-2.5 < \beta_0 < -2.2$ (Figure 3). This is because the youngest stellar population is continuously added to the preexisting populations, keeping the intrinsic stellar UV colour blue. The use of such a set of model SEDs means that the target galaxies' intrinsic stellar SEDs are very blue in the UV with $-2.5 < \beta_0 < -2.2$ (see also Salim & Boquien 2019). It is natural to ask how β_0 distributes among local SFGs?

When model SED templates have β_0 spanning over a reasonably wide range (particularly > -2.2), like given in our declining starburst setting, the recovered β_0 through the SED fitting for our sample of 2 291 local SFGs spreads from -2.4 to -1.7 (median is ~ -2.0). And the best-fitting $\chi^2_{\rm r}$ becomes systematically smaller, compared to the results from the constant starburst fitting. We build new model SED templates by scanning $\tau_{\rm burst}$ from 100 Myr to 10 Gyr (i.e., scanning two values) and perform SED fitting for our sample SFGs to see which set of model SED templates best fit the observed data best. Our results show that about 83 per cent of our sample SFGs are best fitted by the declining starburst model SEDs (i.e., $\tau_{\rm burst} = 100$ Myr). The best-fitting β_0 spreads from -2.5 to -1.7 (median is -2.04) and there are about 85 per cent of galaxies have $\beta_0 > -2.2$. These results indicate that a declining starburst SFH with red UV colour is more favoured by the local SFGs. Indeed, a more complex SFH to generate model SEDs with red intrinsic UV colour of $\beta_0 = -1.9$ is also suggested by Calzetti et al. (2021) for a local galaxy. They pointed out that the starburst regions usually have simple SFHs (e.g. a young instantaneous or constant starburst) and blue UV colours, while the entire galaxies consist of multiple generations of stellar populations (i.e., more complex SFH) usually have redder β_0. Similar results are also reported by Boquien et al. (2012), who modelled galaxy SEDs with free-varied starburst to a sample of local SFGs and obtained the best-fitting β_0 spreading in $-2.2 < \beta_0 < -1.0$.

It is not surprising that the intrinsic UV colour of local SFGs may be red and span a wide range. For instance, Dale et al. (2009) derived β to be in $[-2.3, -0.6]$[9] for metal-poor dwarf galaxies in the Local Volume when $A_{\rm FUV}$ is small (close to 'zero'). Similarly, Battisti et al. (2016) obtained β over $[-2.1, -0.8]$ with a median of -1.6 at 'zero' dust attenuation indicated by the Balmer decrement. One caveat is that the target galaxies in these studies are not representative for those in the regime of high dust attenuation. Nonetheless, we argue that local SFGs should have a rather red and large variation of β_0.

On the other hand, a rather complex SFH with large variation of β_0 was also found in theoretical studies. For example, a theoretical investigation based on the IllustrisTNG simulations predicted a large spread for β_0 among local SFGs, giv-

[9] The original UV slope in Dale et al. (2009) is given as $L_{\rm FUV}/L_{\rm NUV}$. We convert it into β following the empirical relation given by Battisti et al. (2016).

ing $-2.3 < \beta_0 < -1.7$ with a median of -2.07 (Schulz et al. 2020). By analyzing a set of 51 hydrodynamical simulations of selected galaxies, Safarzadeh et al. (2017) gave a similar coverage of β_0 from -2.1 to -1.3 for isolated disc galaxies at $z = 0$. In brief, local SFGs appear to exhibit a large scatter in β_0 (or the intrinsic UV colour).

Back to SED fitting, an SFH having a significant fraction of intermediate-age stellar populations is the key to generate model SEDs with red UV colour (Calzetti et al. 2021). In our two-component SFH prescription, this requirement can be met by adding a declining starburst. If the starburst declines too fast, it fails to supply sufficient recently-formed stars, and the galaxy becomes old and has a lower sSFR; if a constant starburst is involved, the galaxy's UV colour remains blue ($\beta_0 < -2.2$). Our declining starburst recipe sets the e-folding time to 100 Myr and starburst fraction to [0.01, 0.5], being able to generate model SEDs with a reasonably wide coverage of β_0. This is important to reduce the systematic bias in SED fitting induced by the intrinsic UV colour.

6.2 Does the 'true' attenuation curve slope correlate with dust column density?

Our main goal is to address the effects of the degeneracies in SED fitting on the correlation between attenuation curve slope (δ) and dust column density ($\sim A_V$), which has been widely explored using a SED fitting technique in the literature (e.g. Arnouts et al. 2013; Kriek & Conroy 2013; Salmon et al. 2016; Hagen et al. 2017; Leja et al. 2017; Tress et al. 2018; Salim et al. 2018; Decleir et al. 2019; Battisti et al. 2020; Salim & Narayanan 2020; Battisti et al. 2020). We build the observed SEDs for a sample of local SFGs using high-quality multi-wavelength data from the FUV to the FIR and perform SED fitting with reasonable parameter settings. We find that fitting degeneracies induce systematic biases responsible for the correlation between the attenuation curve slope δ and A_V. Our simulation tests further confirm that this correlation is purely controlled by the degeneracy biases in the SED fitting (see Section 4).

Our conclusion disagrees with the interpretation of the A_V–δ relation in S20, which advised the degeneracy errors to be insignificant compared to the global correlation, and A_V as the dominant factor in regulating attenuation curve slope. We reproduced the A_V–δ relation using our sample of local SFGs together with the constant starburst setting in SED fitting, following their settings (see detail in Salim et al. 2018; Salim & Boquien 2019). Our simulation tests demonstrated that the degeneracies between A_V, δ, and β_0 in the SED fitting provoke systematic biases that give rise to a false A_V–δ correlation; a further limitation on the intrinsic UV slope ($-2.5 < \beta_0 < -2.2$) for model SED templates (of constant starburst fitting) strengthens the A_V–δ correlation, and leads to the shrinking of degeneracy errors and the emergence of a A_{FUV}–δ correlation.

In our tests, we started from a fixed attenuation curve slope δ for all mock galaxy SEDs and ended up with a reproduced A_V–δ relation similar to that derived from a sample of local SFGs. The assumption of no correlation between δ and A_V (approximately dust column density) was taken for the mock SFGs. The test results do not exclude the possibility that δ might weakly depend on A_V for star-forming galaxies. When making the input mock galaxy SEDs shaped by an A_V-dependent attenuation curve (either positive or negative), we still obtain an A_V–δ relation having similar slopes as shown in Figure A1. However, it can be distinguished by the dispersion. We find that the dispersion around the relations are 0.21, 0.19 and 0.18 for the mock galaxy SEDs with, satisfying negative, flat and positive input A_V–δ relation, respectively. Compared to the dispersion of 0.18 given in Figure 7, a weak (slope of $\sim$0.2) or no 'true' dependence of δ on A_V is favoured.

On the other hand, the fitting errors only increase the scatter and do not significantly alter the input A_{FUV}–δ relation (the right panels). Thus a rather flat 'true' A_{FUV}–δ relation is favoured. No intrinsic scatter of δ also means a flat 'true' A_V–δ relation (see Figure 8). If the flat A_{FUV}–δ relation has some intrinsic scatter in δ, an increase in δ (by random scatter) towards a larger A_V, i.e., a positive A_V–δ dependence. Specifically, inputting an intrinsic scatter in δ with $\sigma = 0.1$ and 0.2 will result in a positive A_V–δ relation with a slope of 0.3 and 0.8, respectively. However, our mock tests have shown that the dispersion ($\sigma \sim 0.25$) of best-fitting δ can be well recovered if a fixed δ is adopted (i.e., no intrinsic scatter). We inspect that a scattered δ with $\sigma = 0.1$ (0.2) causes a dispersion of $\sigma = 0.25$ (0.30) in output δ. Therefore the intrinsic scatter of δ is expected to have $\sigma < 0.1$, corresponding to an A_V–δ relation with a positive slope of < 0.3. These results suggest that the 'true' A_V–δ relation should be either flat or weakly positive.

One may question if other methods than the energy-balance SED fitting could properly measure galaxy attenuation parameters that are free from the fitting degeneracies. One classical method for determining dust attenuation curve is to compare the attenuated SEDs with the reference 'dust-free' SED (zero attenuation) of a given type of galaxies (Calzetti et al. 1994). Applying this method to a sample of 5 500 local SFGs, Battisti et al. (2017b) found the attenuation curve slope changes little with either stellar mass or metallicity. Both quantities are expected to be good probes of dust attenuation or column density (Garn & Best 2010; Xiao et al. 2012; Qin et al. 2019a; Bogdanoska & Burgarella 2020; Shapley et al. 2021). Similarly, Wild et al. (2011) examined dust attenuation curves using a "pair-matching" method. The galaxy pairs are selected with similar properties but have different dust attenuation. They found that galaxies with higher M_* surface density ($\sim$ higher attenuation) and more face-on ($\sim$ smaller attenuation) tend to have steeper attenuation curves. Rezaee et al. (2021) applied a "direct" method developed by Reddy et al. (2020) to the local SDSS galaxies and found the slope of the (nebular) attenuation curve varies little with either the M_* or metallicity. All these empirical methods have certain shortcomings. Some need to assume that the dusty galaxies and less dusty galaxies have the same intrinsic SEDs. Some measure the attenuation curves of nebular lines, which may be inconsistent with those obtained through SED fitting (i.e. of stars). In any case, if a correlation between attenuation curve slope and dust column density is present, despite of having large scatters, these different methods should give consistent results, which is not seen from those results mentioned above.

In addition, theoretical studies with radiative transfer models often predict a consistent relation between attenuation curve slope and A_V that greyer attenuation curves are coupled with higher dust opacities (Witt & Gordon 2000; Chevallard et al. 2013; Seon & Draine

2016; Narayanan et al. 2018; Trayford et al. 2020; Shen et al. 2020; Salim & Narayanan 2020). The origin of this relationship is the increasing contribution of scattering at lower A_V (Chevallard et al. 2013). However, these radiative transfer predictions depend on the adopted dust-stars distribution geometry. For instance, Lin et al. (2021) found this relationship exists in a well-mixed geometry but is weak or absent if a two-layer geometry is assumed (see also Witt & Gordon 2000). Applying the Empirical Dust Attenuation framework to the large-scale cosmological hydrodynamical simulations (i.e. without radiative transfer effects), Hahn et al. (2021) found that the attenuation curve slope (parameterized by A_{1500}/A_V) flattens with increasing A_V. Given that the physical processes related to dust attenuation are complicated, more efforts are demanded to improve the theoretical modelling of the radiative transfer effects (scattering and absorption) in combination with local geometry effects of the interstellar dust in galaxies, in order to reconcile the theoretical predictions with the observational results.

7 SUMMARY

Using the publicly-available FUV to FIR data, we obtained high-quality SEDs for a sample of 2 291 SFGs selected from the GAMA survey. We carried out SED fitting for our sample SFGs using CIGALE with model SEDs generated from the well-designed declining starburst SFHs, and derived attenuation parameters and examined the effects of the fitting degeneracies between the attenuation curve slope (δ), dust column density ($\sim A_V$) and the intrinsic UV slope (β_0). Our main findings are summarized as follows:

1. The local SFGs exhibit a wide range of β_0 over $[-2.4, -1.7]$ with a median of -2.0. Modelling of galaxy SEDs with model templates from a constant starburst SFH scan a limited range of $\beta_0 < -2.2$, which will significantly bias the determination of attenuation parameters.

2. On average, our local SFGs have attenuation curves slightly steeper than the Calzetti curve with $\delta \approx -0.14$. The variations in best-fitting δ are dominated by the fitting errors.

3. There is a strong degeneracy between β_0 and δ in SED fitting, i.e. the δ–β_0 degeneracy. The current SED fitting algorithm is not able to break this degeneracy and constrain the attenuation curve slope well.

4. We find A_V is strongly degenerate with δ, which strongly biases the measured A_V–δ relation. Instead, A_{FUV} is strictly constrained by the IR luminosity in terms of the energy balance and shows little or no degeneracy with δ. It better measures the dust attenuation than A_V.

5. We find the relation between δ and A_V derived from SED fitting is governed by the systematic biases raised by the fitting degeneracies, but does not reflect an intrinsic connection between the two quantities.

6. The relatively small degeneracy errors given in S20 are attributed to the use of model SED templates generated with constant starburst SFHs in their SED fitting. The model SEDs appear similarly blue in the UV colour ($\beta_0 < -2.2$), and bias the fitting results towards steeper attenuation curves, smaller degeneracy errors, and a stronger A_V–δ correlation.

While the relation between attenuation curve slope and dust column density (e.g. A_V) has been widely explored via the SED fitting algorithm, our principal contribution is to demonstrate that this relation likely finds its origin in the systematic biases driven by fitting degeneracies and chosen model SEDs with biased β_0. We thus argue that the A_V–δ correlation derived from SED fitting, i.e. flatter dust attenuation curves being tightly linked with higher dust attenuation in star-forming galaxies, is no longer valid. More efforts, particularly on the accurate determination of dust attenuation curves, are demanded in the future. Our findings are also useful in guiding interpretations of other fitted parameters in SED studies, which are often degenerate to some level. A hierarchical Bayesian approach may help to break these degeneracies in SED fitting if we have rich multi-wavelength datasets, as demonstrated in some previous studies(e.g., Kelly et al. 2012; Juvela et al. 2013; Galliano 2018; Lamperti et al. 2019).

ACKNOWLEDGMENTS

We are grateful to the anonymous referee for helpful comments and suggestions that significantly improved the quality of the manuscript. This work is supported by the National Key R&D Program of China (2017YFA0402703), the National Science Foundation of China (12073078 and 11773076), the Major Science and Technology Project of Qinghai Province (2019-ZJ-A10), the science research grants from the China Manned Space Project with NO. CMS-CSST-2021-A02, CMS-CSST-2021-A04 and CMS-CSST-2021-A07, and the Chinese Academy of Sciences (CAS) through a China-Chile Joint Research Fund (CCJRF #1809) administered by the CAS South America Centre for Astronomy (CASSACA). SW acknowledges support from the Chinese Academy of Sciences President's International Fellowship Initiative (grant no. 2022VMB0004).

GAMA is a joint European-Australasian project based around a spectroscopic campaign using the Anglo-Australian Telescope. The GAMA input catalogue is based on data taken from the Sloan Digital Sky Survey and the UKIRT Infrared Deep Sky Survey. Complementary imaging of the GAMA regions is being obtained by a number of independent survey programmes including GALEX MIS, VST KiDS, VISTA VIKING, WISE, Herschel-ATLAS, GMRT and ASKAP providing UV to radio coverage. GAMA is funded by the STFC (UK), the ARC (Australia), the AAO, and the participating institutions. The GAMA website is http://www.gama-survey.org/.

DATA AVAILABILITY

The data underlying this article will be shared on reasonable request to the corresponding author.

REFERENCES

Abazajian K. N., et al. 2009, ApJS, 182, 543
Andrae R., Schulze-Hartung T., Melchior P., 2010, arXiv e-prints, p. arXiv:1012.3754
Aoyama S., Hou K.-C., Shimizu I., Hirashita H., Todoroki K., Choi J.-H., Nagamine K., 2017, MNRAS, 466, 105
Arnouts S., et al., 2013, A&A, 558, A67
Asano R. S., Takeuchi T. T., Hirashita H., Nozawa T., 2014, MNRAS, 440, 134
Baldwin J. A., Phillips M. M., Terlevich R., 1981, PASP, 93, 5
Battisti A. J., Calzetti D., Chary R. R., 2016, ApJ, 818, 13
Battisti A. J., Calzetti D., Chary R. R., 2017a, ApJ, 840, 109
Battisti A. J., Calzetti D., Chary R. R., 2017b, ApJ, 851, 90
Battisti A. J., Cunha E. d., Shivaei I., Calzetti D., 2020, ApJ, 888, 108
Bogdanoska J., Burgarella D., 2020, MNRAS, 496, 5341
Boquien M., et al., 2012, A&A, 539, A145
Boquien M., Burgarella D., Roehlly Y., Buat V., Ciesla L., Corre D., Inoue A. K., Salas H., 2019, A&A, 622, A103
Bruzual G., Charlot S., 2003, MNRAS, 344, 1000
Buat V., Giovannoli E., Takeuchi T. T., Heinis S., Yuan F. T., Burgarella D., Noll S., Iglesias-Páramo J., 2011a, A&A, 529, A22
Buat V., et al., 2011b, A&A, 533, A93
Buat V., et al., 2012, A&A, 545, A141
Burgarella D., Buat V., Iglesias-Páramo J., 2005, MNRAS, 360, 1413
Butler R. E., Salim S., 2021, ApJ, 911, 40
Calzetti D., 2001, PASP, 113, 1449
Calzetti D., Kinney A. L., Storchi-Bergmann T., 1994, ApJ, 429, 582
Calzetti D., Armus L., Bohlin R. C., Kinney A. L., Koornneef J., Storchi-Bergmann T., 2000, ApJ, 533, 682
Calzetti D., et al., 2021, ApJ, 913, 37
Cardelli J. A., Clayton G. C., Mathis J. S., 1989, ApJ, 345, 245
Chabrier G., 2003, PASP, 115, 763
Charlot S., Fall S. M., 2000, ApJ, 539, 718
Chevallard J., Charlot S., Wandelt B., Wild V., 2013, MNRAS, 432, 2061
Clayton G. C., Gordon K. D., Bianchi L. C., Massa D. L., Fitzpatrick E. L., Bohlin R. C., Wolff M. J., 2015, ApJ, 815, 14
Cortese L., Boselli A., Franzetti P., Decarli R., Gavazzi G., Boissier S., Buat V., 2008, MNRAS, 386, 1157
Dale D. A., et al., 2009, ApJ, 703, 517
Decleir M., et al., 2019, MNRAS, 486, 743
de Jong J. T. A., et al., 2013, The Messenger, 154, 44
Doore K., Eufrasio R. T., Lehmer B. D., Monson E. B., Basu-Zych A., Garofali K., Ptak A., 2021, ApJ, 923, 26
Draine B. T., 2003, ARA&A, 41, 241
Draine B. T., Lee H. M., 1984, ApJ, 285, 89
Draine B. T., Li A., 2007, ApJ, 657, 810
Driver S. P., et al., 2009, Astronomy and Geophysics, 50, 5.12
Driver S. P., et al., 2011, MNRAS, 413, 971
Driver S. P., et al., 2016, MNRAS, 455, 3911
Eales S., et al., 2010, PASP, 122, 499
Ferland G. J., Korista K. T., Verner D. A., Ferguson J. W., Kingdon J. B., Verner E. M., 1998, PASP, 110, 761
Ferland G. J., et al., 2013, Rev. Mex. Astron. Astrofis., 49, 137
Ferreras I., et al., 2021, MNRAS, 505, 283
Fitzpatrick E. L., Massa D., 1986, ApJ, 307, 286
Gallazzi A., Charlot S., Brinchmann J., White S. D. M., Tremonti C. A., 2005, MNRAS, 362, 41
Galliano F., 2018, MNRAS, 476, 1445
Galliano F., Galametz M., Jones A. P., 2018, ARA&A, 56, 673
Garn T., Best P. N., 2010, MNRAS, 409, 421
Giovannoli E., Buat V., Noll S., Burgarella D., Magnelli B., 2011, A&A, 525, A150
Gordon K. D., Clayton G. C., Misselt K. A., Landolt A. U., Wolff M. J., 2003, ApJ, 594, 279
Gordon Y. A., et al., 2017, MNRAS, 465, 2671
Guo K., Zheng X. Z., Wang T., Fu H., 2015, ApJ, 808, L49
Guthrie B. N. G., 1992, A&AS, 93, 255
Hagen L. M. Z., Siegel M. H., Hoversten E. A., Gronwall C., Immler S., Hagen A., 2017, MNRAS, 466, 4540
Hahn C., et al., 2021, arXiv e-prints, p. arXiv:2106.09741
Han Y., Han Z., 2014, ApJS, 215, 2
Han Y., Han Z., 2019, ApJS, 240, 3
Hirashita H., 2012, MNRAS, 422, 1263
Hopkins A. M., et al., 2013, MNRAS, 430, 2047
Hou K.-C., Hirashita H., Nagamine K., Aoyama S., Shimizu I., 2017, MNRAS, 469, 870
Inoue A. K., 2011, MNRAS, 415, 2920
Iyer K. G., et al., 2020, MNRAS, 498, 430
Juvela M., Montillaud J., Ysard N., Lunttila T., 2013, A&A, 556, A63
Kashino D., et al., 2021, ApJ, 909, 213
Kauffmann G., et al., 2003, MNRAS, 346, 1055
Kelly B. C., Shetty R., Stutz A. M., Kauffmann J., Goodman A. A., Launhardt R., 2012, ApJ, 752, 55
Kelvin L. S., et al., 2012, MNRAS, 421, 1007
Kennicutt R. C., Evans N. J., 2012, ARA&A, 50, 531
Kewley L. J., Jansen R. A., Geller M. J., 2005, PASP, 117, 227
Kirkpatrick A., Pope A., Sajina A., Roebuck E., Yan L., Armus L., Díaz-Santos T., Stierwalt S., 2015, ApJ, 814, 9
Koprowski M. P., et al., 2020, MNRAS, 492, 4927
Kriek M., Conroy C., 2013, ApJ, 775, L16
Lamperti I., et al., 2019, MNRAS, 489, 4389
Leja J., Johnson B. D., Conroy C., van Dokkum P. G., Byler N., 2017, ApJ, 837, 170
Li N., et al., 2021, ApJ, 917, 72
Lin Z., Kong X., 2020, ApJ, 888, 88
Lin Y.-H., Hirashita H., Camps P., Baes M., 2021, MNRAS, 507, 2755
Liske J., et al., 2015, MNRAS, 452, 2087
Małek K., et al., 2018, A&A, 620, A50
Mao Y.-W., Kennicutt Robert C. J., Hao C.-N., Kong X., Zhou X., 2012, ApJ, 757, 52
Martin D. C., et al., 2005, ApJ, 619, L1
Mathis J. S., 1994, ApJ, 422, 176
Mullaney J. R., Alexander D. M., Goulding A. D., Hickox R. C., 2011, MNRAS, 414, 1082
Narayanan D., Conroy C., Davé R., Johnson B. D., Popping G., 2018, ApJ, 869, 70
Nersesian A., et al., 2019, A&A, 624, A80
Noll S., Burgarella D., Giovannoli E., Buat V., Marcillac D., Muñoz-Mateos J. C., 2009, A&A, 507, 1793
Padilla N. D., Strauss M. A., 2008, MNRAS, 388, 1321
Pei Y. C., 1992, ApJ, 395, 130
Pettini M., Pagel B. E. J., 2004, MNRAS, 348, L59
Qin J., Zheng X. Z., Wuyts S., Pan Z., Ren J., 2019a, MNRAS, 485, 5733
Qin J., Zheng X. Z., Wuyts S., Pan Z., Ren J., 2019b, ApJ, 886, 28
Reddy N. A., et al., 2015, ApJ, 806, 259
Reddy N. A., et al., 2020, ApJ, 902, 123
Ren J., et al., 2022, MNRAS, 510, 3071
Rezaee S., Reddy N., Shivaei I., Fetherolf T., Emami N., Khostovan A. A., 2021, MNRAS, 506, 3588
Safarzadeh M., Hayward C. C., Ferguson H. C., 2017, ApJ, 840, 15
Salim S., Boquien M., 2019, ApJ, 872, 23
Salim S., Narayanan D., 2020, ARA&A, 58, 529 (S20)
Salim S., et al., 2016, ApJS, 227, 2
Salim S., Boquien M., Lee J. C., 2018, ApJ, 859, 11
Salmon B., et al., 2016, ApJ, 827, 20
Schlegel D. J., Finkbeiner D. P., Davis M., 1998, ApJ, 500, 525

Schulz S., Popping G., Pillepich A., Nelson D., Vogelsberger M., Marinacci F., Hernquist L., 2020, MNRAS, 497, 4773
Seon K.-I., Draine B. T., 2016, ApJ, 833, 201
Shapley A. E., et al., 2021, arXiv e-prints, p. arXiv:2109.14630
Sharma S., 2017, ARA&A, 55, 213
Shen X., et al., 2020, MNRAS, 495, 4747
Shivaei I., et al., 2020, ApJ, 899, 117
Sparre M., Hayward C. C., Feldmann R., Faucher-Giguère C.-A., Muratov A. L., Kereš D., Hopkins P. F., 2017, MNRAS, 466, 88
Taylor E. N., et al., 2011, MNRAS, 418, 1587
Teklu B. B., Lin Z., Kong X., Wang E., Gao Y., Liu Q., Hu N., Liu H., 2020, ApJ, 893, 94
Trayford J. W., Lagos C. d. P., Robotham A. S. G., Obreschkow D., 2020, MNRAS, 491, 3937
Tress M., et al., 2018, MNRAS, 475, 2363
Weingartner J. C., Draine B. T., 2001, ApJ, 548, 296
Wild V., Charlot S., Brinchmann J., Heckman T., Vince O., Pacifici C., Chevallard J., 2011, MNRAS, 417, 1760
Witt A. N., Gordon K. D., 1996, ApJ, 463, 681
Witt A. N., Gordon K. D., 2000, ApJ, 528, 799
Wright E. L., et al., 2010, AJ, 140, 1868
Wright A. H., et al., 2016, MNRAS, 460, 765
Xiao T., Wang T., Wang H., Zhou H., Lu H., Dong X., 2012, MNRAS, 421, 486
Yuan F.-T., Burgarella D., Corre D., Buat V., Boquien M., Shen S., 2019, A&A, 631, A123
Zeimann G. R., et al., 2015, ApJ, 814, 162

APPENDIX A: ADDITIONAL FIGURES

This paper has been typeset from a TEX/LATEX file prepared by the author.

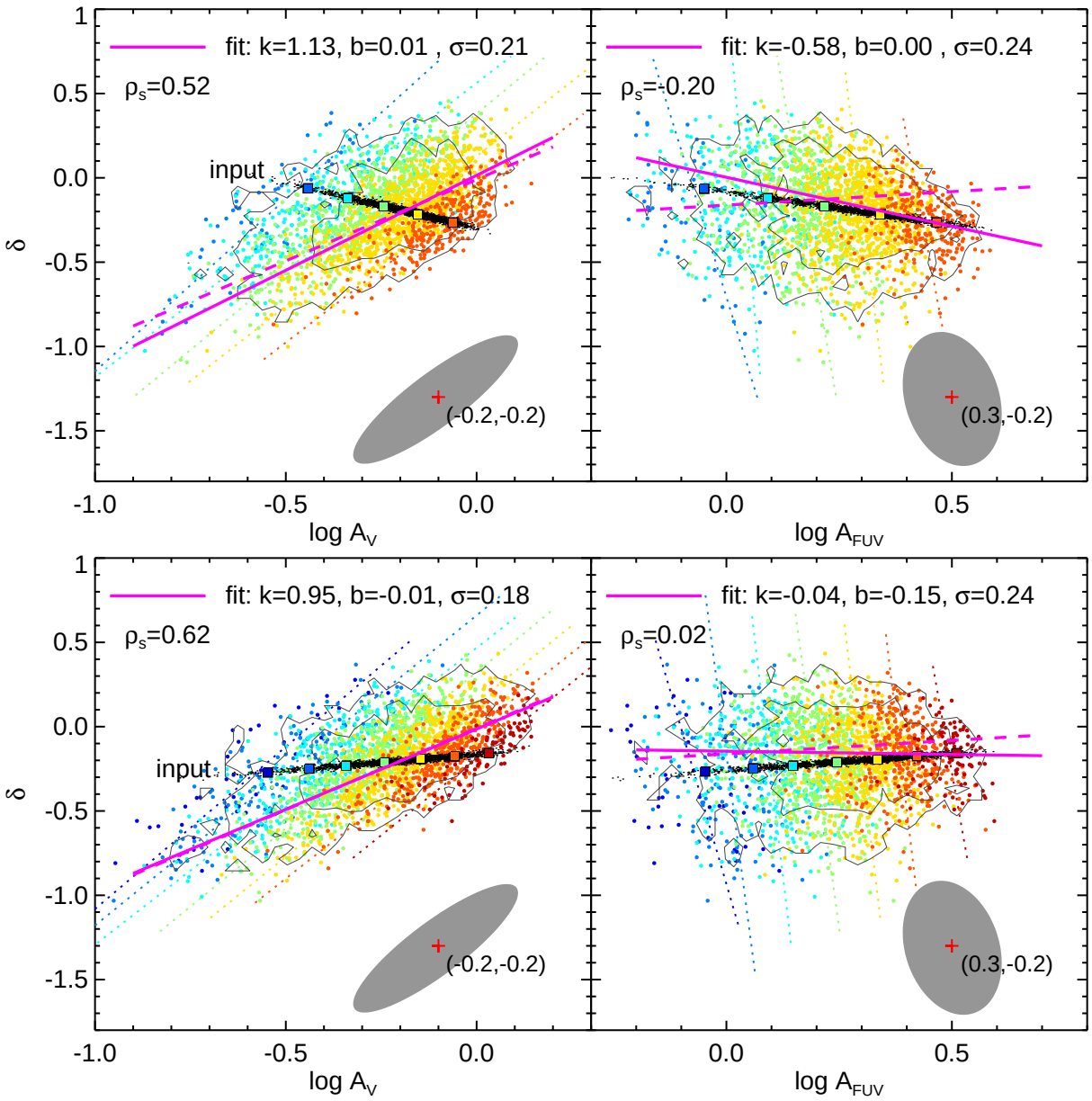


Figure A1. Similar to Figure 8 but showing the results of simulated galaxies having a negative (top, slope $\sim$−0.5) and positive (bottom, slope $\sim$0.2) input A_V–δ relation, respectively.